

In-situ real-time evolution of intrinsic stresses and microstructure during growth of cathodic arc deposited (Al,Ti)N coatings

Sanjay Nayak¹, Tun-Wei Hsu¹, Lina Rogström¹, Maiara Moreno¹, Jon M. Andersson², Mats P. Johansson-Jöesaar^{1,2}, Robert Boyd¹, Norbert Schell³, Jens Gibmeier⁴, Jens Birch¹, and Magnus Odén¹

¹Department of Physics, Chemistry and Biology (IFM), Linköping University, SE-581 83 Linköping, Sweden

²Seco Tools AB, 737 82, Fagersta, Sweden

³Helmholtz-Zentrum Hereon, Institute of Materials Physics, Max-Planck-Str. 1, Geesthacht 21502, Germany

⁴Institute for Applied Materials, Materials Science and Engineering (IAM-WK), Karlsruhe Institute of Technology, 76131, Karlsruhe, Germany

Abstract

The residual stress plays a vital role in determination of the device performance that uses thin films coating and thus the accurate determination of stress and its optimization with process parameters is an ongoing research work for many decades. In line with this, the microscopic origin of the stress at the atomic scale and its development during the thin film deposition is a matter of major scientific interests. The development of stress is a complex phenomenon and has a complex dependence to process parameters, film microstructure and its morphology. In this work, by utilizing a custom-designed cathodic arc deposition system and synchrotron radiation based 2D x-ray diffraction (XRD) technique, we determine the real-time evolution of stress, crystallite sizes and their preferential orientations of Aluminum-Titanium-Nitride ($\text{Al}_x\text{Ti}_{1-x}\text{N}$) films with varied Al-content ($x=0.0, 0.25, 0.50, \text{ and } 0.67$) on Si-100 substrate. The energies of incoming ions and hence stress in the films is tuned by applying different direct current substrate bias ($V_s = \text{floating potential, } -20, -40, -60, -80, \text{ and } -100 \text{ V}$). The instantaneous stress is evaluated by the well-known $d \text{ vs. } \sin^2\psi$ technique, while crystallite sizes are determined by analyzing line profiles of x-ray diffractograms. The evolution of stress and crystallite sizes are modelled with multiple numerical models from which kinetic parameters associated with the thin film depositions are extracted. The ex-situ microstructure characterizations of $\text{Al}_x\text{Ti}_{1-x}\text{N}$ coatings are carried out by scanning electron microscopy (SEM) and transmission electron microscopy (TEM). The formation of ex-situ microstructure of the films is discussed considering the results obtained from in-situ XRD data. Finally, we demonstrate that the method utilized here is a powerful approach towards estimation of the fracture toughness of thin film coatings.

I. INTRODUCTION:

Thin film coatings are the building blocks of today's technology. Their applications are widespread, such as in, semiconductor devices [1,2], optoelectronics [3], micro and nano electromechanical systems [4], detectors [5], energy storage [6], optical mirrors [7], and wear and corrosion-resistant coating [8], etc. Since thin film are deposited over a lattice-mismatched surface of a single crystalline substrate material, they are often strained. In addition, the deposition process is a non-equilibrium phenomenon, leading to the generation of residual stresses in the coatings [9]. This residual stress plays a vital role in the performance during their application. While a high value of tensile stress leads to cracking [10], compressive stress can cause buckling, blistering, and delamination of the coatings [11–13]. Thus, accurate determination and optimization of stress in the thin film is of great technological importance, and hence over the last 100 years it has been pursued [14,15]. The strain/stress is also an important external parameters that can enabled many material properties, such as electrical and thermal conductivity [16], ferroelectricity [17], piezoelectricity [18], optical properties [19], mechanical hardness [20,21], etc. Besides their post-deposition stress determination, understanding the evolution of stress during their deposition is of scientific interest.

There are various methods for the determination of residual stresses in coatings, such as wafer curvature measured by multibeam optical stress sensors (MOSS) [9], synchrotron x-ray diffraction [22], holographic transmission electron microscopy (TEM) [23], micro-Raman spectroscopy [24], and electron diffraction [25]. Amongst all, largely MOSS has been successfully used in the in-situ evaluation of stress during thin film depositions. While MOSS is very powerful in determining the macroscopic stress of the entire films for both crystalline as well as amorphous samples, it will not reveal any information about microstructure evolution. In contrast, x-ray diffraction can provide both in-situ strain and information on microstructure simultaneously, but it is limited to only crystalline materials. Using MOSS, the study of stress evolution during the growth of polycrystalline thin films is extensively investigated, but most of them are on pure metal films on insulator substrates only [26–29]. In addition, a few reports are available where MOSS was used to study the stress evolution in a complex compound system, such as transition metal nitrides [30–33]. However, all these nitrides thin films were deposited with a relatively lower deposition rate technique, such as magnetron sputtering.

Polycrystalline thin film of multi-component alloys of transition metals nitrides (TMNs), particularly (Al,Ti)N-based coatings are the current workhorse of the cutting tool industry. The success of the (Al,Ti)N materials system compared to traditional TiN hard coatings has been attributed to 1) increased oxidation resistance with increasing aluminium content [34]; and 2) the associated age-hardening effect with elevating working temperature, due to the formation of coherency strains between c-TiN and metastable c-AlN domains by spinodal decomposition [35]. For superior oxidation resistant and enhanced thermomechanical properties, a higher concentration of Al is preferable, but the aluminium content in cubic-(Al,Ti)N is limited to $\approx 65\%$ due to thermodynamic limitations [36,37]. Above 65% of Al content, the formation of additional hexagonal (Al,Ti)N crystallizes, which has inferior mechanical properties compared to the cubic phase [38,39]. The mechanical properties and consequently the tool's performance is also influenced by the microstructure of the coating, i.e., the grain size, density, grain orientation, dislocation density, etc. Suggested by the Hall-Petch relation[40], that above a critical grain size the hardness of the overall coating material increases with decreasing grain size. A common approach to modify the grain size can be accomplished by energetic ion bombardments, which are controlled by applying a negative electrical bias to the substrate surface [39,41]. The physical vapour depositions process especially in cathodic arc evaporation comprises a high density of metal ions and multiple charge states, thus their kinetic energy can be increased substantially by applying a negative DC bias to the substrate [42]. Upon bombardment of these high-speed ions on top of already growing surfaces of the films can modify the stress level as well as the orientation of the grains in the polycrystalline thin films[43,44]. Such a change in the preferred orientation strongly correlates to its mechanical properties, [45–49] hence also its performance during the actual service conditions [50,51].

Although cathodic arc deposition is the industrial preferred technique for (Al,Ti)N-based coatings, the evolution of microstructure and strain/stress during deposition are still not well understood and scarcely studied. Here we present the in-situ real-time evolution of coating stress and microstructure during growth of ultra-high vacuum (UHV) cathodic arc deposited (Al,Ti)N alloy coatings as a function of substrate bias (V_s). Both the stress state and microstructure of the coatings were evaluated and analysed by synchrotron x-ray diffractograms recorded during film growth. All depositions were carried out in a specially designed UHV deposition system, adapted for synchrotron radiation studies [52].

II. EXPERIMENTAL DETAILS:

Alloyed (Al,Ti)N coatings with varied Al-content ($\text{Al}_x\text{Ti}_{1-x}\text{N}$) on Si (100) substrate are deposited by reactive cathodic arc deposition technique, where the deposition system is schematically shown in Figure 1. 63 mm diameter size metallic Ti (Grade-2), and alloys of $\text{Al}_{0.25}\text{Ti}_{0.75}$, $\text{Al}_{0.50}\text{Ti}_{0.50}$, and $\text{Al}_{0.67}\text{Ti}_{0.33}$ (FK-Grade) are used as cathodes. The cathode current is fixed at 75 A for all depositions.

The cathodes are mounted on home-designed holders, which are further mounted on a specially designed chamber lid [52]. The angle between the surface normal of the cathodes to the substrate normal is 35° (see Figure 1). The distance between the substrate and the cathode is ≈ 12 cm. Pure (99.9995%) nitrogen (N_2) flow is introduced into an ultra-high vacuum system with a base pressure of 10^{-8} Torr. During the deposition of all $Al_xTi_{1-x}N$, the growth pressure is fixed at 40 mTorr. Prior to deposition the Si (100) substrate is cleaned by ultrasonic bath with isopropyl alcohol and dried by blowing dry air. For all depositions, the substrate is heated up to $450^\circ C$ by an 808 nm infrared laser diode (Dilas Diode Laser, Inc.) powered by a 300 W power supply (Lumina Power, Inc.). The laser beam is focused on a susceptor material, here silicon carbide (SiC), which then heats the substrate via thermal conduction and radiation. The substrate is rotated at a speed of 5 rotations per minute (RPM). The applied voltage in electrical bias to substrate (V_s) is applied by using a DC power supply, and is varied between the depositions from -20 to -100 V in steps of -20 V. In addition, depositions at floating potential (FP) are also performed. The duration of the deposition of all coatings is fixed at 10 minutes. During the experiments, the deposition chamber was fixed to a high-resolution hexapod with a resolution in x/y/z movement of $\pm 1 \mu m$.

The film microstructure and final thickness is determined from a fractured cross-sectional view using a FESEM (Leo 1550 Gemini) operated at 5 kV. Microstructural characterization of the coatings was made by TEM and STEM using an FEI Tecnai G220 UT microscope operated at 200 kV. In-situ x-ray diffractograms of $Al_xTi_{1-x}N$ coatings are recorded in transmission mode during the deposition of the coatings by utilizing synchrotron radiation at the P07 High Energy Materials Science (HEMS) beamline at PETRA III (Deutsches Elektronen-Synchrotron (DESY); Hamburg, Germany). The energy of the x-ray photons is selected to 73.79 keV. The beam slit widths are fixed at $100 \times 600 \mu m^2$. The diffractograms are recorded with a 2D flat panel detector with 2048×2048 pixels (PerkinElmer XRD 1622). The exposure time for recording one diffractogram is 0.2 s, and ten such patterns are superposed with each other to generate a final diffractogram. The distance between substrate and detector is evaluated by recording the diffractogram of NIST standard LaB_6 powder. In this set of experiments, the distance is determined to be 3.373 m. The detector was positioned to collect one quadrant of the diffraction pattern for optimizing the resolution.

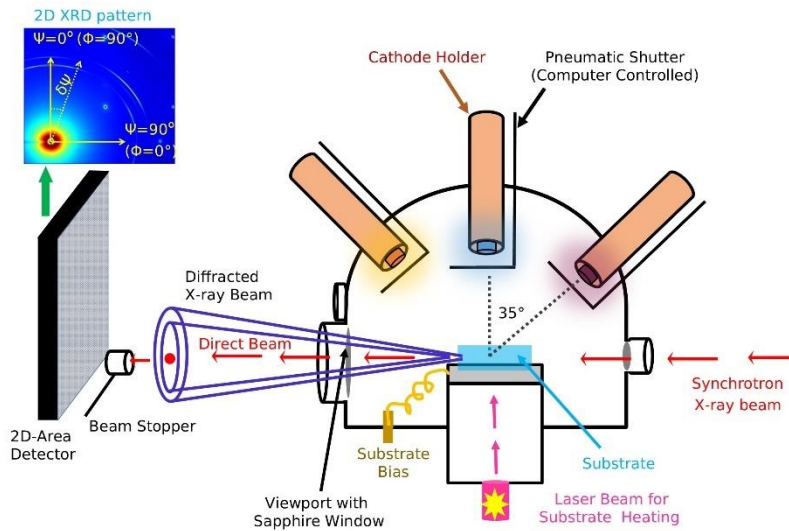


Figure 1. The sketch of the experimental setup of our experiments. The angle between substrate's surface normal and the normal to cathode targets surface is 35° . The relationship between Φ and ψ is also shown in the 2D- XRD pattern.

The 2-dimensional XRD patterns are transformed into one-dimensional lineouts by integration in $\approx 5^\circ$ - 8° wide azimuthal bins (ψ). The interplanar lattice spacing (d_{hkl}) is determined by fitting the one-dimensional lineout with a pseudo-Voigt function. The details of the method used in estimation of in-plane strain and biaxial stress is given in section SI. I of supplementary information (SI). In determination of stress, high temperature ($450^\circ C$) elastic constants of $Al_xTi_{1-x}N$ are used (see Ref. [53] and section SI. I of SI for details).

The crystallite size is approximated to coherently diffracting domains ($\langle D_{hkl} \rangle$), and at a film thickness, t_f , ($\langle D_{hkl}(t_f) \rangle$) is estimated using the Debye-Scherrer formula [54].

$$\langle D_{hkl}(t_f = t) \rangle = \frac{0.9 \times \lambda}{\zeta(t_f = t) \cos \theta(t_f = t)} \quad (1)$$

Where λ is the wavelength of the x-ray beam, $\zeta(t_f = t)$ and $\theta(t_f = t)$ are the the instrumental broadening corrected FWHM of the one-dimensional lineouts in radians and half of diffraction angle, 2θ , of hkl crystal planes at $t_f = t$, respectively. The

instrumental broadening was determined from the FWHM of the diffraction signal from the LaB₆ powder. The $\langle D_{hkl} \rangle$ of Al_xTi_{1-x}N coatings along the GD (D_{111}^{GD}) as deposited with different V_s are obtained by integrating the intensity of diffractograms from $\psi = 0^\circ$ to 10° of c-111 crystal planes. Evolutions of D_{111} along the IP-direction (D_{111}^{IP}) are obtained by measuring line width profiles of the diffractograms formed close to the IP-direction of c-111 crystal planes. The respective values of range of ψ used in integration of diffraction intensities are mentioned in the later sections.

The evolution of average crystallite size, $\langle D_{hkl}(t_f) \rangle$ with the film thickness t_f , along the in-plane direction is modelled with a power law as follows.

$$\langle D_{hkl}(t_f) \rangle = k \times t_f^n \quad (2)$$

The evolution of film thickness, t_f , average σ as a function of t_f is modelled using a power law,

$$\langle \sigma(t_f) \rangle = \sigma_0 + c \times t_f^{-\nu} \quad (3)$$

The σ_0 are the converged $\langle \sigma(t_f) \rangle$ at large t_f . The scaling parameter c and ν are the coefficients related to the rate of grain boundary shrinkage with an exponent of ν [55]. The σ evolution of Al_xTi_{1-x}N coatings is also modelled using a recently developed kinetic model proposed by Chason *et al.* [56] and is given by:

$$\begin{aligned} \langle \sigma(t_f = t) \rangle = & \sigma_c + \left(\frac{\sigma_{T,0}(L_0)}{L(t_f = t)^{0.5}} - \sigma_c \right) \times \exp(-\beta D_{\text{eff}}/RL(t_f = t)) + A \left(\frac{1}{L(t_f = t)} \right) \\ & + \left(1 - \frac{1}{L(t_f = t)} \right) \times B \times \frac{1}{\left(1 + \frac{1}{R\tau_s} \right)} \quad (4) \end{aligned}$$

where σ_c is the compressive stress that is generated by the insertion of ions at the grain boundary, which is fixed at -0.02 GPa in our work [30]. $\sigma_{T,0}(L_0)$ is the tensile stress generated by the formation of a new segment of grain boundaries with a grain size of L_0 . $L(t_f = t)$ is the average grain size at $t_f = t$, approximated to in-plane $\langle D_{hkl}(t_f) \rangle$ in our fitting. β is a parameter that depends upon the mechanical properties of the layer and concentration of mobile defects. D_{eff} is the effective diffusivity of atoms from surface to grain boundary. R is the rate at which grain boundary height is changing, which is approximated by the film growth rate in our work. The third and fourth terms of Eqn. 4 represent stress due to energetic vapour fluxes. The third term is related to collision-induced densification of grain boundary, while the last term is due to the formation of defects in bulk with a depth of l from the surface. Parameter τ_s is the characteristic time at which defects created in bulk migrate to the surface and annihilate. The parameter τ_s is further approximated to,

$$\tau_s = \frac{1}{R} \left[\alpha - 1 - \alpha \sqrt{1 - \frac{2}{\alpha}} \right]$$

where $\alpha = D_i/2Rl$. D_i represent the diffusivity of the defect created in bulk. Parameters A and B are adjustable parameters. In this work, a least-squares method is used to fit Eqn.3 and 4 to the experimentally obtained data. While fitting of Eqn. 7 is named as Model 1, fitting of experimental σ with Eqn. 8 will be named as Model 2 in the rest of this paper. In fitting of Model 2 to the experimental data, A and B are restricted to have a negative value. While σ_c is fixed at -0.2 GPa for all compositions of Al_xTi_{1-x}N, $\sigma_{T,0}(L_0)$ is tuned to get a better fitting, but kept fixed for one composition, i.e., 0.67 GPa, 0.85 GPa, 1.00 GPa, and 2.50 GPa for $L_0 = 100$ nm in TiN, Al_{0.25}Ti_{0.75}N, Al_{0.50}Ti_{0.50}N, Al_{0.67}Ti_{0.33}N, respectively. Quality of fitting of both Model 1 and Model 2 are assessed by a R-squared (R^2) analysis.

III. FORMATION AND EVOLUTION OF MICROSTRUCTURE:

A. Formation of crystal phases, and crystallographic texture

Recorded diffractograms of all samples at the end of deposition are displayed in Figure 2. The corresponding Miller indices of different diffraction spots/rings are identified by measuring interplanar distances (or corresponding 2θ values) and are marked

accordingly. $\text{Al}_x\text{Ti}_{1-x}\text{N}$: $x \leq 0.5$ coatings show the formation of only cubic crystal phases (c-) (see Figure 2 (a-o)), while $\text{Al}_{0.67}\text{Ti}_{0.33}\text{N}$ coatings grown with $|V_s| \leq 60$ V show mixed cubic and hexagonal phases (h-) (see Figure 2 (p-r)). At a higher V_s (i.e., -80 and -100 V) no detectable hexagonal phases of $\text{Al}_x\text{Ti}_{1-x}\text{N}$ are seen (see Figure 2 (s-u) and Figure S-6 (a) of SI).

TiN coating deposited at $V_s = \text{FP}$ shows a preferred orientation of c-111 planes along the growth direction (GD), along with a minority component at an angle of $\psi \approx 74^\circ$ to the growth direction (see Figure 2 (a)). The angle between the (111) and (200) directions in a cubic crystal is $\sim 55^\circ$, corresponding well to the preferred orientation seen for the c-200 rings (see Figure 2 (a)). TiN coatings deposited with $V_s = -20$ V and -40 V, the crystallites in the films orient more randomly, but higher intensity diffraction spots are present in c-200 ring at an angle of $\psi \approx 22^\circ/20^\circ$ and $\psi \approx 70^\circ/77^\circ$ (see Figure 2 (b-c)). TiN samples deposited at $V_s = -60, -80,$ and -100 V show the formation of the preferred orientation of crystallites with c-111 along the GD and intense diffraction from c-200 appears close to a $18^\circ\text{--}20^\circ$ inclination angle to the GD (see Figure 2 (d-f)). The texture of c-200 at close to $\psi \approx 70^\circ$ is consequent of the 90° rotational symmetry of the c-200 crystal planes in the FCC lattice.

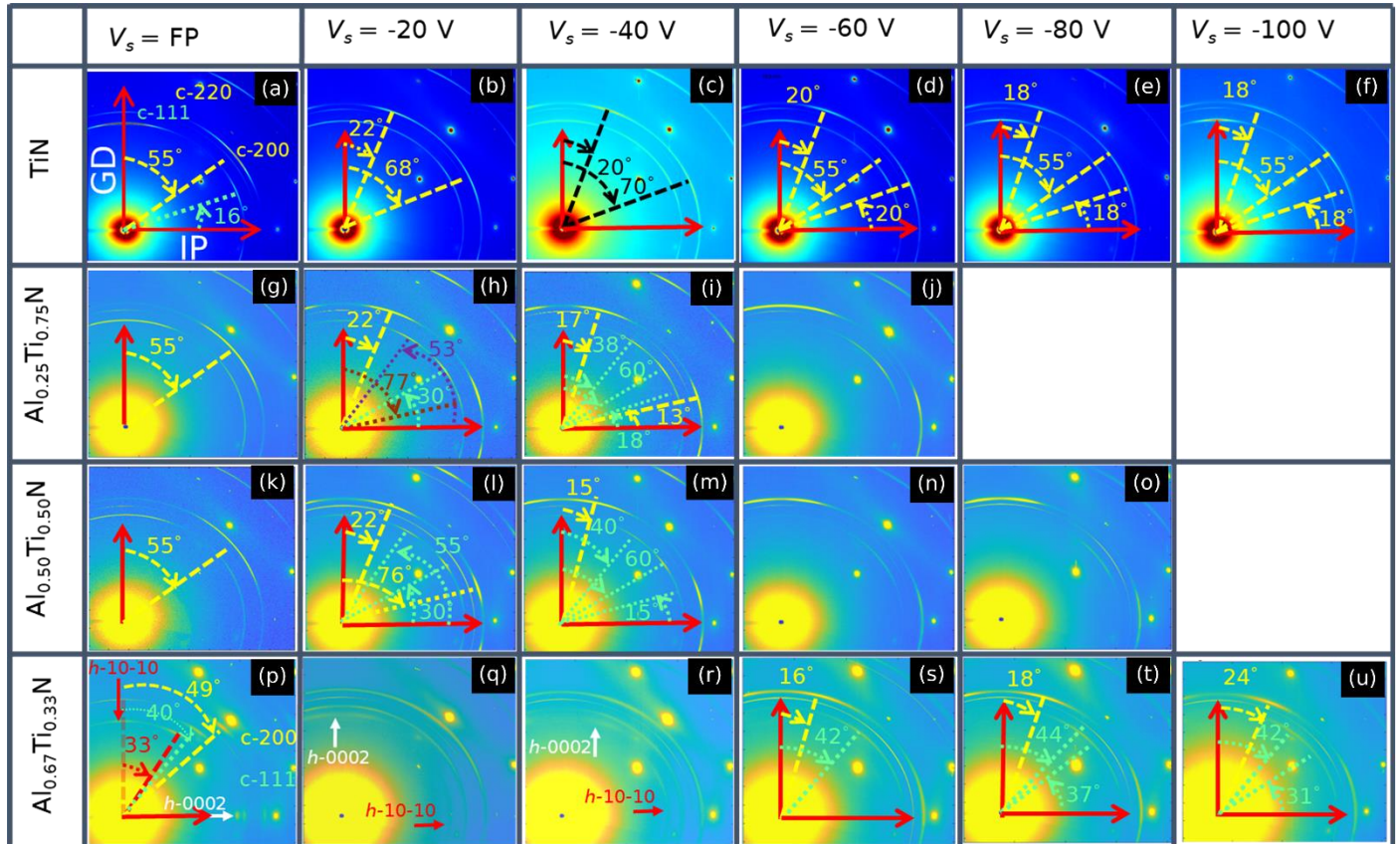


Figure 2. 2D x-ray diffractograms of $\text{Al}_x\text{Ti}_{1-x}\text{N}$ coatings deposited on Si (100) substrate at different substrate bias voltages (V_s). Diffraction from hkl planes of cubic phases is denoted as c-hkl, while for hexagonal phases they are denoted as h-hkil where $i = -(h+k)$. The unmarked high intensities spots are from Si substrates.

The $\text{Al}_{0.25}\text{Ti}_{0.75}\text{N}$ coating deposited at $V_s = \text{FP}$ shows a preferred orientation of c-111 along the GD and c-200 at an angle $\psi \approx 55$ (see Figure 2 (g)). With $V_s = -20$ V, the orientation of c-200 planes splits along two distinct ψ orientations: (i) one at $\psi \approx 22^\circ$ and (ii) at $\psi \approx 77^\circ$ (see Figure 2 (h-i)). There are three distinct intense regions in the c-111 Debye ring: (i) at $\psi \approx 37^\circ$, (ii) at $\psi \approx 60^\circ$, and (iii) at $\psi \approx 77^\circ$. The application of V_s also influenced the texture of c-111 crystallographic planes. The diffractograms of $\text{Al}_{0.25}\text{Ti}_{0.75}\text{N}$ coatings for both $V_s = -20$ and -40 V are similar, except in the latter case the c-200 crystal planes are tilted a bit closer towards the GD with a tilt angle of 17° . The intense spots of c-111 at an angle $\psi \in [37^\circ, 40^\circ]$ are from the crystallographic c-111 planes of the grains which c-200 planes are inclined at angle of $\psi \in [-15^\circ, -20^\circ]$. The intense spots of c-111 at an angle $\approx 60^\circ$ are from the same grains for which c-200 planes are at an inclined angle close to $\psi \in [+15^\circ, +20^\circ]$. The intense c-111 close $\psi \approx 75^\circ$ is from different grains altogether, whose c-200 diffraction spots should be close to $\psi \approx 45^\circ$, i.e., tilted away from the GD. A faint c-200 in these regions indicate the grain volume of these grains are smaller. With further increase in V_s to -60 V the c-200 crystal planes are found to be along the GD with a broader azimuthal distribution (see Figure 2 (j)). Note that the $\text{Al}_{0.25}\text{Ti}_{0.75}\text{N}$ coating deposited with $V_s = -60$ V shows a cohesive failure to the substrate during its film deposition. Similar behaviour in the diffractogram of $\text{Al}_{0.50}\text{Ti}_{0.50}\text{N}$ is

also seen. The coatings deposited at $V_s = -60$ V and -80 V both show a predominant texture of c-200 along the GD and cohesive failure of the coatings (discussed later) (see Figure 2 (n-o)).

Unlike the above-discussed compositions of $Al_xTi_{1-x}N$: $x \leq 0.5$, the diffractograms from $Al_{0.67}Ti_{0.33}N$ coatings show a different crystallographic texture formation. Formation of both hexagonal and cubic phase crystals are noticed (see Figure 2(p-u) and Figure S-6 of SI). X-ray diffractograms recorded from $Al_{0.67}Ti_{0.33}N$ coating deposited with $V_s = FP$ show $h-10\bar{1}0$ crystal planes are aligned along the GD and at an inclined angle of 33° to the GD (see Figure 2 (p)). A clear and sharp diffraction spot corresponding to $h-0002$ planes is in parallel to the IP direction (see Figure 2 (p)). The c-111 and c-200 crystal planes of $Al_{0.67}Ti_{0.33}N$ are inclined at an angle 40° and 49° to the GD, respectively. Weakly textured c-111 and c-200 crystal planes of c-AlTiN phases are also seen along the IP (see Figure 2 (p)). Since the angle between these two c-111 and c-200 is not in agreement with the crystallographic angle ($\approx 55^\circ$) between c-111 and c-200 in FCC lattice, we suggest both are from two distinct grains with different orientations. Based on analysis of symmetry of the crystal structure, we find that the c-200 crystal planes of the grains whose c-111 planes are at an angle of 40° to the GD should be at around 95° from the GD [hence 5° from the IP direction]. And the c-111 planes of grains whose c-200 are at inclined angle of 49° to the GD should be at around 84° from the GD. Presence of diffraction spots of c-111 and c-200 along and close to the IP direction agrees well with this prediction. With $V_s = -20$ and -40 V, the crystal planes' orientation changes dramatically. The crystallographic orientation of c-111 and c-200 planes are random, along with $h-0002$ and $h-10\bar{1}0$ planes oriented along the GD and towards the IP direction, respectively (see Figure 2 (q-r)). Surprisingly, for $Al_{0.67}Ti_{0.33}N$ coatings deposited with $|V_s| \geq 60$ V, no sign of diffractograms corresponding to hexagonal phase are observed (see Figure 2 (s-u)). The intense spots of the Debye ring corresponding to c-200 crystal planes of $Al_{0.67}Ti_{0.33}N$ are at an angle 16° , 18° , and 24° to the GD for coatings deposited at $V_s = -60$, 80 , and 100 V, respectively. The c-111 planes are orientated at an angle of $42^\circ/44^\circ$ to the GD for all films (see Figure 2 (s-u)). A fixed tilt angle of intense of c-111 and varied c-200 clearly establish that both intense diffraction patterns are originated from different grains with different orientations.

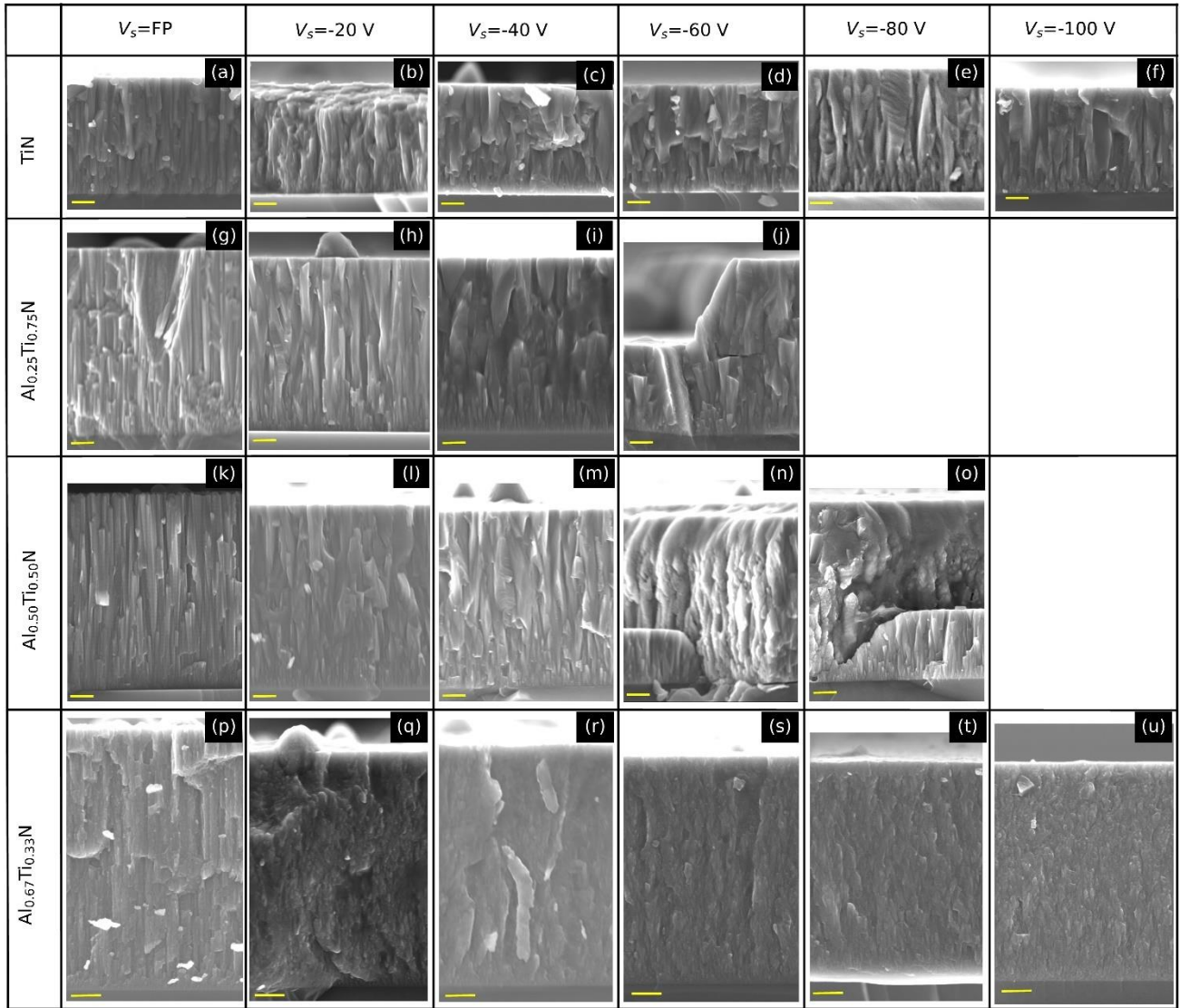
B. Ex-situ surface morphology, film thickness, and growth rate

Cross-section SEM micrographs revealed that all films have a columnar structure (see Figure 3). The total film thickness t_f of $Al_xTi_{1-x}N$ coating, determined from the cross-sections viewed in the SEM, are tabulated in Table 1. The TiN coating grown at $V_s = FP$ shows the formation of relatively smaller domain size, and loosely packed nanocolumns with gaps (voids) between neighbour nanocolumns at the bottom part of the coating extending to the top. With an increase in $|V_s|$ (≥ 20 V) during the thin film deposition, the TiN coatings densify with a larger domain size of nanocolumns. A closer look into the cross-sectional SEM images of TiN coatings deposited with a finite V_s reveals the formation of individual thin NCs until t_f of ≈ 200 - 300 nm beyond which they coalescence to form broad nanocolumns (NCs).

Similar morphology evolution under different V_s is observed for $Al_{0.25}Ti_{0.75}N$ and $Al_{0.50}Ti_{0.50}N$. A major difference in the cross-sectional morphologies of $Al_{0.25}Ti_{0.75}N$ and $Al_{0.50}Ti_{0.50}N$ coatings deposited at $V_s = FP$ is noticed where in the latter case the nanocolumns are more isolated than the former one. $Al_{0.25}Ti_{0.75}N$ and $Al_{0.50}Ti_{0.50}N$ coatings deposited above $|V_s| \geq 60$ V show characteristic features of a coating with cohesive failure that occurred during the film deposition. In these films two distinct t_f can be seen (see Figure 3 (j, n, and o)). The electron micrographs obtained from $Al_{0.67}Ti_{0.33}N$ coating differ from those with lower Al content. While $Al_{0.67}Ti_{0.33}N$ films grown at $V_s = FP$ a nanocolumnar structure is seen, with an applied V_s the cross-sectional SEM image shows a densely packed nanocrystalline like morphology.

Table 1 Total film thickness (t_f) of $Al_xTi_{1-x}N$ coatings deposited with different substrate bias voltage (V_s). The deposition time is fixed for 10 minutes.

V_s (V)	t_f (nm)			
	TiN	$Al_{0.25}Ti_{0.75}N$	$Al_{0.50}Ti_{0.50}N$	$Al_{0.67}Ti_{0.33}N$
FP	1007(± 12)	1631(± 12)	1640(± 20)	1867(± 12)
-20 V	917(± 8)	1494(± 10)	1545(± 15)	1573(± 15)
-40 V	920(± 8)	1508(± 10)	1508(± 12)	1677(± 11)
-60 V	912 (± 8)	1471(± 10)	1545(± 10)	1615(± 11)
-80 V	930(± 10)	-	1520(± 10)	1508(± 10)
-100 V	895(± 10)	-	-	1502(± 15)



*Scale bar 200 nm

Figure 3 shows fractured cross-sectional FESEM micrographs of $\text{Al}_x\text{Ti}_{1-x}\text{N}$ coatings deposited on Si (100) substrate at different substrate bias voltage (V_s). The scale bar is 200 nm.

Planview SEM micrographs of the TiN coatings grown at $V_s = \text{FP}$ and -20 V reveal a platelet-like surface morphology with the presence of nanometre size pores in coating grown with FP substrate bias (see dotted red circles in Figure S-2 of SI). TiN coatings grown with $|V_s| \geq 40 \text{ V}$ shows granular morphology indicating the formation of faceted nanocolumns. Surface morphologies of for $\text{Al}_{0.25}\text{Ti}_{0.25}\text{N}$ coatings deposited at $V_s = \text{FP}$ and -20 V are similar to the TiN coatings deposited at the same V_s . But coatings deposited at $|V_s| \geq 40 \text{ V}$ are different from those of TiN, where the top of nanocolumns are faceted but relatively flatter than those of TiN. Plan view SEM of $\text{Al}_{0.50}\text{Ti}_{0.50}\text{N}$ coating grown with $V_s = \text{FP}$ shows a clear view of sharp pyramidal faceted nanocolumns with the clear presence of voids between them. At higher V_s , the surface morphologies are compact and flat faceted. Unlike $\text{Al}_x\text{Ti}_{1-x}\text{N}$: $x \leq 0.5$, surface morphologies of $\text{Al}_{0.67}\text{Ti}_{0.33}\text{N}$ are granular and with the increase in bias the domain sizes of coatings are finer. Low magnification SEM images show cohesive failure and in-plane spallation of coatings (see Figure S-3 of SI).

To get a deeper insight into the microstructure, we probed the microstructure of TiN coatings ($V_s = \text{FP}$ and -40 V) with ex-situ TEM (see Figure 4). Clearly, below t_f of 400 nm the domain sizes are different from those above it (see Figure 4 **Error! Reference source not found.** (a-1 and b-1)). Towards the interfaces of coatings and substrate the domain sizes are smaller, and their number densities are higher compared to the top of the coatings. With t_f larger than 400 nm, the in-plane domain sizes of the TiN coating deposited with $V_s = \text{FP}$ is almost constant at $\sim 100 \text{ nm}$ (see Figure 4 (a-1)). A closer look at the top of the coatings reveal that a few nanocolumns are separated from each other by a few nanometres size gaps (see arrow marked region of Figure 4 (a-2)). The selected area electron diffraction (SAED) pattern from overall region of films and substrate reveal a spotty diffractogram suggesting

formation of crystalline and textured grains (see Figure 4 (a-3)). The predominant c-111 diffraction along the GD agrees with our in-situ XRD, suggesting no change in the grain orientation during the cooling down of the coatings as well as post-deposition. HR-TEM images recorded close to the interface of coating and substrate revealed that crystallites formed at t_f close to ≈ 2 nm are having an interplanar spacing close to 0.21 nm, and hence crystal planes are identified as c-200 (see Figure 4 (a-4)). The c-200 crystal planes are oriented at an angle close to $\approx 55^\circ$ to the direction normal to coating/substrate interfaces (see Figure 4 (a-4)). Comparing the 2D x-ray diffractograms recorded at the end of deposition (see Figure 2 (a)) along with the HRTEM image (see Figure 4 (a-4)) suggests, that from a t_f of ≈ 2 nm, c-200 planes of TiN deposited with $V_s = \text{FP}$ remains at an angle close to 55° to the GD. An intracolumnar grain boundary is presented, see Figure 4 (a-5), indicating a distinct (see Figure 4 (a-4)) c-200 grains oriented in two different ψ -directions. The red triangle indicates an area of the sample which has an amorphous-like structure. Unlike TiN deposited at $V_s = \text{FP}$, the intercolumnar gap vanished in coatings deposited with $V_s = -40$ V (see arrow marked region in Figure 4 (b-2)). We also noticed that at t_f lower than 400 nm, a large density of nanocolumn's growth is terminated (see arrow marked columns in Figure 4 (b-1)), beyond which a dense coating is seen. SAED patterns (see Figure 4 (b-3)) revealed a diffractogram corresponding to the random orientation of crystal structure, corroborating our XRD pattern (see Figure 2 (c)). HRTEM image from the coating/substrate interfaces region further revealed a poor crystalline quality of the grains and their random orientation exist from the initial stages of the deposition onwards. Furthermore, we probed the intracolumnar grain boundary (see arrow marked in Figure 4 (b-5)), which suggests that the grain boundaries are sharp and crystalline.

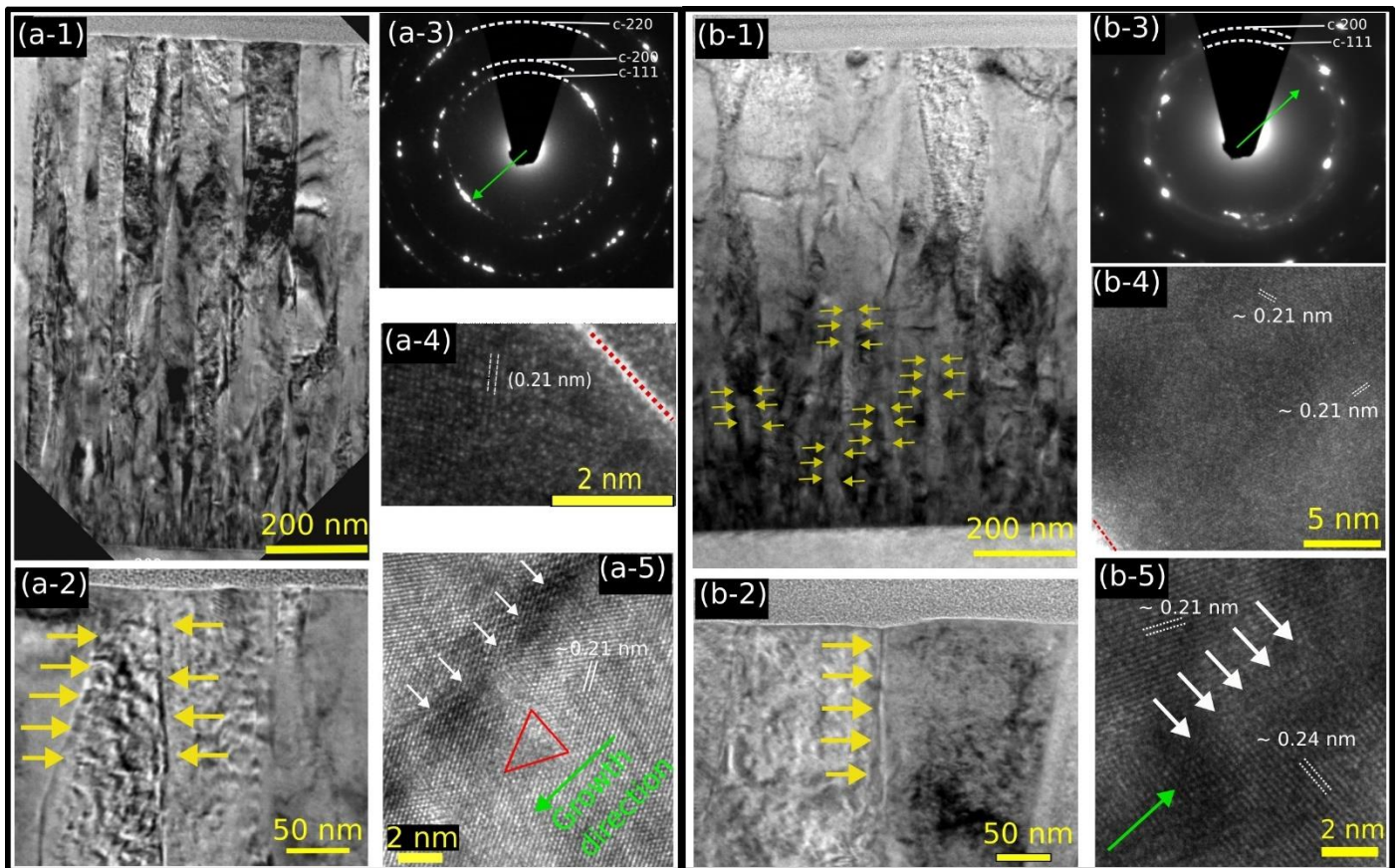


Figure 4 is the TEM analysis of TiN coatings deposited at substrate bias voltage (V_s) of FP (a-1 to a-4), and -40 V (b-1 to b-4). Figure a-1 and a-2 are TEM images, a-3 is the SAED pattern, a-4, is the HRTEM image recorded at the interfaces of the coating and Si(100) substrate and a-5 a HRTEM image from the intracolumnar grain boundary. Figure b-1 and b-2 are TEM images of TiN coating deposited at a substrate bias voltage (V_s) of -40 V. Figure b-3 is the SAED pattern, b-4 is an HRTEM image of the interface, and b-5 is the intracolumnar grain boundary. The green coloured arrows depict the growth direction. Diffraction signal from the cubic phase is indexed in the SAED patterns. The red-coloured dashed line in b-4 represents the line of interfaces.

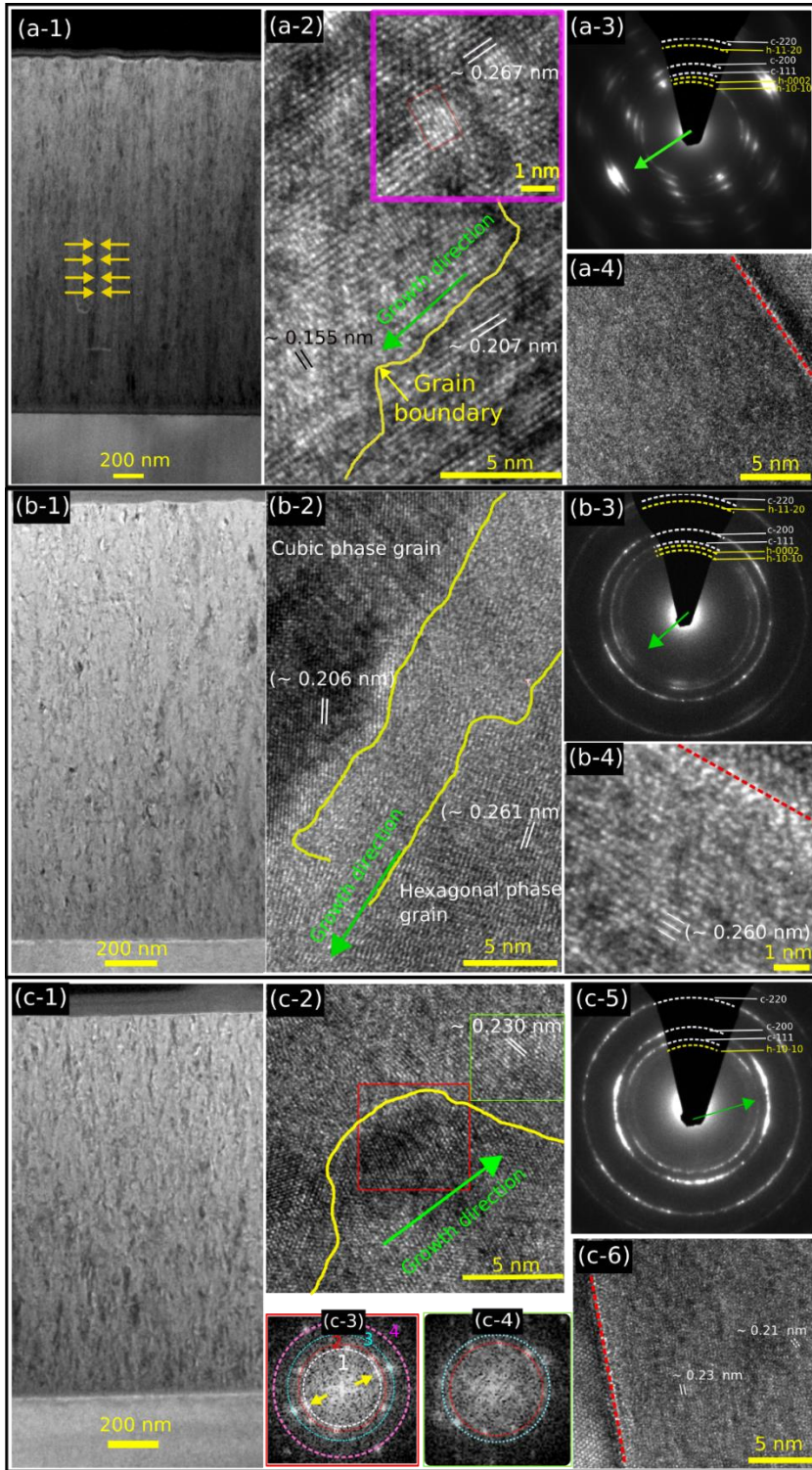


Figure 5 the TEM analysis of $Al_{0.67}Ti_{0.33}N$ coatings deposited at substrate bias voltage (V_s) of FP (a-1 to a-4), -40 V (b-1 to b-4), and -80 V (c-1 to c-6). Figure a-1 is BF-TEM image, a-2 is an HRTEM image, a-3 the SAED pattern, and a-4 an HRTEM image recorded at the interface of the coating and Si(100) substrate. The inset of figure a-2 (area within the pink square) shows a cubic domain (within the red rectangle) separated and grain boundary, where formation of hexagonal phases are noticed. Figure b-1 is a BF-TEM image, b-2 a HRTEM image, b-3 is the SAED pattern, b-4 is an HRTEM image from the interface. Figure c-1 is the BF-TEM image and c-4 is an HRTEM image. Figure c-3 and c-4 are the FFT pattern of the region within the red square and green rectangle in c-2, respectively. The circle marked as 1, 2, 3, and 4 in figure c-3 are corresponding FFT patterns from $h-10\bar{1}0$, c-111, c-200, and c-220 crystal planes, respectively. and c-5 is the SAED pattern. c-6 is an HRTEM image of the interface. The green coloured arrow depicts the growth direction. The red coloured dashed line represents the interface between coating and substrate.

Ex-situ microstructure of $Al_{0.67}Ti_{0.33}N$ coatings [$V_s = FP, -40 V, \text{ and } -80 V$] are further studied using TEM (see Figure 5). A *nanocrystalline* -like morphology is confirmed for $Al_{0.67}Ti_{0.33}N$ coatings (see Figure 5 a-1, b-1, and c-1)). While $Al_{0.67}Ti_{0.33}N$ coatings deposited with $V_s = -40$ and $-80 V$ are dense (see Figure 5 (b-1, and c-1)), an intercolumnar space is quite noticeable in coating deposited with $V_s = FP$ (see Figure 5 (a-1)). The presence of both hexagonal and cubic phases is further confirmed by both HRTEM and SAED. $Al_{0.67}Ti_{0.33}N$ coatings deposited with $V_s = FP$ and $-40 V$ show the formation of hexagonal phases (see Figure 5 (a-2, a-3, b-2, b-3)). The formation of very small hexagonal and cubic domains is seen in $Al_{0.67}Ti_{0.33}N$ coating deposited with $V_s = FP$ (see inset of Figure 5 (a-2)). The interplanar spacing of 0.267 nm is corresponding to $h-0002$ of $Al_{0.67}Ti_{0.33}N$, which is aligned along IP direction (see inset of Figure 5 (a-2)) in agreement with our XRD (see Figure S-6 (a) of SI). The region marked with a red rectangle is corresponding to the cubic domain with c-220 ($d_{220} = 0.155$ nm) crystal planes aligned along the GD (see inset of Figure 5 a-2)). . We also find that a distinct grain boundary between cubic and hexagonal phases exists along with a grain boundary between

differently oriented cubic phases of $\text{Al}_{0.67}\text{Ti}_{0.33}\text{N}$ (see Figure 5 (a-2)). SAED patterns along with the HRTEM, of $\text{Al}_{0.67}\text{Ti}_{0.33}\text{N}$ coating deposited with $V_s = \text{FP}$, suggest that the $h\text{-}10\bar{1}0$, $h\text{-}11\bar{2}0$ and $c\text{-}220$ crystal planes are also oriented along the GD. This is in contrast with the crystal orientation of $\text{Al}_x\text{Ti}_{1-x}\text{N}$: $x \leq 0.5$, deposited at $V_s = \text{FP}$, coatings, where 111 crystallographic planes of cubic $\text{Al}_x\text{Ti}_{1-x}\text{N}$ are oriented along the GD. Based on these observations we conclude that the orientation of crystallographic orientation in $\text{Al}_x\text{Ti}_{1-x}\text{N}$ alloys in polycrystalline thin film form is not only constrained by geometry of the deposition system but can be influenced by the composition of the coatings too, especially in the compositions where mixed phases of crystals can form. Further inspection of HRTEM images of $\text{Al}_{0.67}\text{Ti}_{0.33}\text{N}$ coating with $V_s = \text{FP}$, near coating/substrate interface regions, suggests the presence of an amorphous-like region (see Figure 5 a-4)).

Similar to $\text{Al}_{0.67}\text{Ti}_{0.33}\text{N}$ coating deposited with $V_s = \text{FP}$, for coating deposited with $V_s = -40$ V, grain boundary between hexagonal and cubic phases are also seen (see Figure 5 (b-2)). However, the region in between the grain boundaries (as depicted between yellow lines in Figure 5 (b-2)) is either an amorphous-like region or crystalline in which zone-axis is not aligned with the beam directions. Nevertheless, a clear presence of grain boundaries is noticed. The recorded SAED pattern for coating with $V_s = -40$ V is a bit different than that of the coating with $V_s = \text{FP}$. The diffraction intensities from hexagonal phases are faint compared to cubic phases (see Figure 5 b-3)), further corroborating our XRD findings (see Figure 2(p)). The dominant crystallographic orientations are no longer $c\text{-}220$ and $h\text{-}11\bar{2}0$, but rather $c\text{-}200$ along the GD. The faint $h\text{-}11\bar{2}0$ pattern appears along the in-plane (see Figure 5 (b-3)). HRTEM images recorded close to the interface of coating/substrate revealed the formation of small crystallites with an interplanar spacing of ≈ 0.260 nm corresponding to interplanar spacing of $h\text{-}0002$ crystal planes of $\text{Al}_{0.67}\text{Ti}_{0.33}\text{N}$, and they are oriented along the GD, further corroborating our XRD findings.

In $\text{Al}_{0.67}\text{Ti}_{0.33}\text{N}$ coating deposited at $V_s = -80$ V, our XRD data show a complete absence of hexagonal phases. However, the ex-situ SAED pattern revealed the presence of a very faint $h\text{-}10\bar{1}0$ pattern with no preferential orientations (see Figure 5 (c-5)). No detectable $h\text{-}0002$ or $h\text{-}11\bar{2}0$ signal is seen. A careful investigation of HRTEM images reveal that hexagonal phases are formed at the grain boundary region only. The fast-Fourier transformation (FFT) of the HRTEM image around a grain boundary (see the red squared area in Figure 5 c-2)) shows the presence of $h\text{-}10\bar{1}0$ spots (see spots aligned with circle denoted as 1 in Figure 5 c-3)). The FFT pattern (see Figure 5 c-4)) obtained from an individual grain (green squared area of Figure 5 (c-4)) revealed a complete absence of any spots corresponding to the hexagonal phases. Thus, we conclude that for $\text{Al}_{0.67}\text{Ti}_{0.33}\text{N}$ coatings deposited at higher V_s [e.g., -80 and -100 V], the hexagonal phase nucleates only at grain boundaries, but not in the bulk of the grains. Further, an HRTEM image taken at the interface between coatings and substrate revealed the formation of very small crystallites with $c\text{-}200$ crystal planes oriented along the GD, and $c\text{-}111$ inclined with an angle of close to 45° (see Figure 5 c-6)) [$\approx 44^\circ$ measured from XRD]. This observation establishes that the crystal planes of the coatings seen at very small film thickness ($\sim 2\text{-}3$ nm) retain their crystallographic orientation throughout the deposition.

To further understand the temporal evolution (i.e., average grain size as a function of film thickness increases) of the above-discussed grain (also crystallite) sizes and their orientation (i.e., texture) during the thin film depositions, we analysed the line profiles and diffraction intensities of the recorded diffractograms. While the thickness-dependent evolution of x-ray diffractograms and their evolution along the GD is thoroughly discussed in the section SI. III of SI, we dedicate the next section to the evolution of the grain/crystallite sizes.

C. Temporal evolution of crystallite size (D_{hkl})

Many film properties such as, film hardness and stress evolution strongly connected to the grain size of the coatings. Thus, here we evaluate the temporal evolutions of crystallite size ($\langle D_{hkl} \rangle$) of $\text{Al}_x\text{Ti}_{1-x}\text{N}$ with different V_s along the GD (see Figure S-9 of SI) as well as close to the IP direction (see Figure 6 (a-d)). For all compositions, the respective ranges of ψ values that are used for integrating the diffraction intensities to obtain the line profiles are mentioned on top of each figure (see Figure 6). While here we discuss the crystallite size evolution along the *in-plane* direction, details of the same along GDs are discussed in section SI. IV of SI.

We find that a power-law like (see Eqn. 2) increase in average D_{111} as film thickness increases is noticed for $x = [0,0.5]$ in $\text{Al}_x\text{Ti}_{1-x}\text{N}$. Thin films of $\text{Al}_x\text{Ti}_{1-x}\text{N}$: $x = [0,0.5]$ deposited with $V_s = \text{FP}$, shows a rapid increase in D_{111} as t_f increases as compared to films deposited with a finite applied V_s (see Figure 6(a-c)). For example, at $t_f \approx 200$ nm, D_{111}^{IP} of TiN deposited at $V_s = \text{FP}$ is estimated to ≈ 23 nm and increased to ≈ 38 nm at $t_f = 1007$ nm while film deposited at $V_s = -20$ V at the end of depositions ($t_f \approx 920$ nm) D_{111}^{IP} is estimated to ≈ 37 nm. With further increase in V_s to -40, -60, -80, and -100 V, D_{111}^{IP} of TiN at the end of depositions are ≈ 29 nm, ≈ 30 nm, ≈ 33 nm, and ≈ 33 nm, respectively (see Figure 6 (a)). Similar behaviour on the evolution of D_{111}^{IP} in $\text{Al}_{0.25}\text{Ti}_{0.75}\text{N}$ and $\text{Al}_{0.50}\text{Ti}_{0.50}\text{N}$ coatings is seen. Thin film of $\text{Al}_{0.25}\text{Ti}_{0.75}\text{N}$ deposited with $V_s = \text{FP}$ increases from ≈ 19 nm [$t_f \approx 200$ nm] to ≈ 41 nm [$t_f \approx 1631$ nm] (see Figure 6 (b)). With $V_s = -20$ V, D_{111}^{IP} is estimated to ≈ 23 nm at $t_f \approx 200$ nm and increases to ≈ 33 nm as

t_f reaches to 1494 nm (see Figure 6 (b)). A similar evolution of D_{111}^{IP} is observed for $V_s = -40$ V. At $t_f \approx 200$ nm, D_{111}^{IP} is estimated to ≈ 22 nm, while as t_f reaches to 1494 nm, D_{111}^{IP} is ≈ 33 nm. Likewise, the texture evolution of $Al_{0.25}Ti_{0.75}N$ at $V_s = -60$ V (see Figure S-9(b) of SI), a discontinuity in evolution of D_{111}^{IP} is also observed at $t_f \approx 770$ nm (see Figure 6 (b)). The D_{111}^{IP} at $t_f \approx 200$ nm is ≈ 24 nm, while at $t_f \approx 770$ nm it is estimated to be ≈ 27 nm in this case. Similar to $Al_{0.25}Ti_{0.75}N$ coatings the evolutions of D_{111}^{IP} vs. t_f in $Al_{0.50}Ti_{0.50}N$ coatings deposited with $V_s = -60$ and -80 V show an abrupt change at $t_f \approx 950$ nm and 745 nm, respectively (see Figure 6 (c)). At $t_f \approx 150$ nm, D_{111}^{IP} of $Al_{0.50}Ti_{0.50}N$ coating deposited at $V_s = -60$ is estimated to ≈ 18 nm, while at $t_f \approx 950$ nm D_{111}^{IP} is 25 nm. D_{111}^{IP} of $Al_{0.50}Ti_{0.50}N$ coating deposited at $V_s = -80$ V changes from 16 nm to 23 nm, as t_f increases from ≈ 150 nm to ≈ 1545 nm.

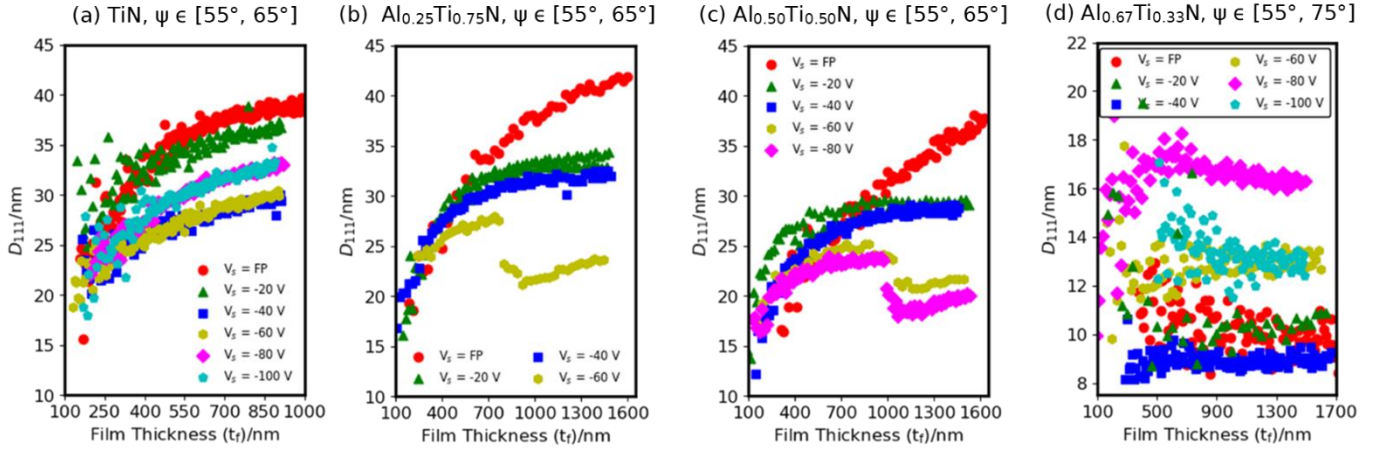


Figure 6 (a-d) are the temporal evolution of crystallite size (D_{hkl}) of $Al_xTi_{1-x}N$ close to in-plane direction. Thin film coatings are deposited on $Si(100)$ substrate at various substrate bias voltages. The range of tilt angle (ψ) used to integrate the intensity of XRD patterns in transforming 2D XRD to 1D line-out are shown on top of each figure.

The D_{111}^{IP} of $Al_{0.67}Ti_{0.33}N$ coatings are estimated by integrating the diffraction intensities from c-111 crystal planes within the ψ ranges of $55-75^\circ$ (see Figure 6 (d)). $Al_{0.67}Ti_{0.33}N$ coating deposited with $V_s = FP$, estimated D_{111}^{IP} at $t_f \approx 400$ nm is ≈ 11 nm, which reduced to ≈ 9.5 nm at $t_f \approx 1867$ nm. Estimated D_{111}^{IP} of $Al_{0.67}Ti_{0.33}N$ coating with $V_s = -20$ V is 10.5 nm at all t_f . The evolution of D_{111}^{IP} of $Al_{0.67}Ti_{0.33}N$ coating deposited with $V_s = -40$ V is a bit complex. From $t_f \approx 280$ nm to ≈ 650 nm, a small increase in D_{111}^{IP} from 8.6 nm to 9.6 nm is noticed. Beyond $t_f \approx 650$ nm, D_{111}^{IP} decreases to 8.6 nm and almost remains constant thereafter. With $V_s = -60$ V, D_{111}^{IP} remains almost constant at 12.9 nm. The average D_{111}^{IP} of $Al_{0.67}Ti_{0.33}N$ coating with $V_s = -60$ V is again a bit complex. We observe between the $t_f \approx 120-550$ nm that D_{111}^{IP} increases from 11.4 nm to 17.5 nm. Beyond $t_f \approx 550$ nm, D_{111}^{IP} decreases with an increase in t_f , and at $t_f \approx 1508$ nm D_{111}^{IP} is estimated to be 16.5 nm. The estimated D_{111}^{IP} of $Al_{0.67}Ti_{0.33}N$ coating deposited with $V_s = -100$ V is 14.5 nm at $t_f \approx 500$ nm, and it decreases to 13 nm at $t_f \approx 1502$ nm. The evolutions of D_{111}^{IP} vs. t_f for all samples are fitted with Eqn. 2, and the coefficients (k) and exponents (n) are tabulated in Table S-2 of SI.

Next, to uncover the effect of compositions and substrate bias (and consequently the formation and evolution of different microstructures as discussed in previous sections) to the stress evolutions of the films, the temporal evolution of the thickness averaged stress is determined (see section II and section SI. I of SI for details of evaluation method). As mentioned in section II, the film thickness, t_f , averaged stress is modelled with different two numerical equations. Below we presented evolution of internal stress (determined from internal strain, see Method section) in TiN , $Al_{0.25}Ti_{0.75}N$, $Al_{0.50}Ti_{0.50}N$, and $Al_{0.67}Ti_{0.33}N$ in four different sub-sections of section IV.

IV. EVOLUTION OF BIAxIAL STRAIN AND STRESS

A. Titanium nitride (TiN)

We determined both biaxial IP strain ($\epsilon_{\psi=90^\circ}$) and GD strain ($\epsilon_{\psi=0^\circ}$) using the diffractograms from c-111 crystal planes of all coatings and monitored their temporal evolution (see Figure S-11 of SI). The biaxial stress (σ) is shown in Figure 7. The negative sign (-) in the strain/stress values indicate all TiN films are experiencing a compressive strain/stress. The positive (+) sign during

thin film deposition represents tensile strain/stress. In these experiments, we could assess stress/strain from diffractograms recorded for $t_f \geq 200$ nm only, due to too low intensity at lower thicknesses.

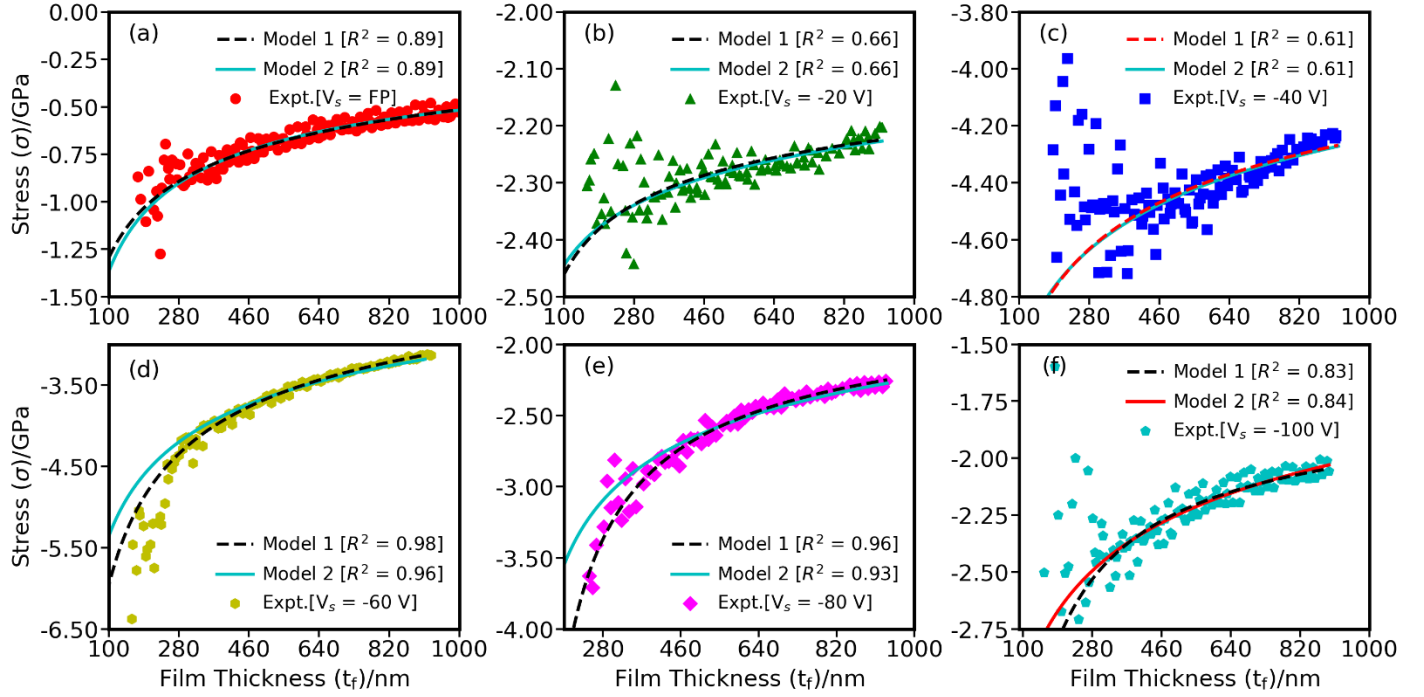


Figure 7 is the biaxial stress ($\langle \sigma_{111} \rangle$) evolution of TiN on Si (100) substrate at different substrate bias voltages V_s ; at floating potential (a), -20 V (b), -40 V (c), -60 V (d), -80 V (e), and -100 V (f). Experimentally obtained data are fitted with a power law (Model 1, dashed line) and a kinetic model (Model 2, solid lines) as discussed in section II.

For TiN, deposited at all V_s , the final σ is always compressive. At $t_f \approx 280$ nm, σ of TiN coatings deposited at $V_s = \text{FP}$, -20, -40, -60, -80, and -100 V are approximately -0.8, -2.3, -4.5, -4.3, -3.0, and -2.5 GPa, respectively. At the very end of the deposition, the σ (and t_f) is estimated as -0.5 GPa (≈ 1007 nm), -2.2 GPa (≈ 917 nm), -4.2 GPa (≈ 920 nm), -3.1 GPa (≈ 912 nm), -2.2 GPa (≈ 930 nm), and -2.0 GPa (≈ 895 nm) for $V_s = \text{FP}$, -20, -40, -60, -80, and -100 V, respectively. This suggests a “U” type behaviour of final values of σ in TiN films with increase in V_s . We use the power law (presented in Eqn. 3) to fit the σ vs. t_f (see dashed lines (Model 1) in Figure 7). The fitted co-efficient and exponents for TiN coatings with varying V_s are tabulated Table 2. It shows that, the parameter σ_0 , to which $\sigma(t_f)$ converge was found to be positive (0.54 GPa) for coating deposited with $V_s = \text{FP}$, while for coatings deposited with V_s of -20, -40, -60, -80 and -100 V, the σ_0 is negative but have a U type dependence to the V_s (see Table 2). The coefficient c , which is related to the stress generated or shrinkage by grain boundaries, [55,57] is always a negative number. The values of γ are close to 0.20 with $V_s = \text{FP}$, -20, and -40V and consistently increases with further increases in V_s (see Table 2). We note that for TiN coatings deposited at $V_s = -20$ and -40 V, the estimated stress in between 280-460 nm is a bit dispersed, suggesting a wider distribution of stress present in the coatings at such lower t_f .

Table 2 Least squares optimized pre-factors and exponents obtained by fitting the evolution of stress ($\langle \sigma_{111} \rangle$) vs. t_f in $\text{Al}_x\text{Ti}_{1-x}\text{N}$ with Eqn. 3 (Model 1).

V_s (V)	σ_0 (GPa)				c (GPa nm $^\gamma$)				γ			
	$x=0.0$	$x=0.25$	$x=0.50$	$x=0.67$	$x=0.0$	$x=0.25$	$x=0.50$	$x=0.67$	$x=0.0$	$x=0.25$	$x=0.50$	$x=0.67$
FP	0.54	0.52	0.83	1.1	-5.54	-3.47	-8.93	3474.1	0.24	0.2	0.37	1.29
-20	-1.80	-0.77	-0.94	-1.3	-1.66	-2.19	-6.18	3474.1	0.20	0.2	0.46	1.35
-40	-2.91	-2.24	-2.01	-3.2	-5.32	-2.97	-16.38	3474.1	0.20	0.2	0.56	1.35
-60	-1.03	-4.28	-3.10	-4.3	-29.07	-2.52	-84.70	3474.1	0.38	0.2	0.60	1.58
-80	-1.56	∅	∅	-5.8	-49.90	∅	∅	-6.1	0.63	∅	∅	0.25
-100	-1.66	∅	∅	∅	-45.08	∅	∅	∅	0.70	∅	∅	∅

The σ vs. t_f of TiN coatings are further analysed within the kinetic model proposed by Chason *et al.* [56], which is briefly discussed in section II. The σ_c and $\sigma_{T,0}$ ($L=100$ nm) are fixed at -0.02 and 0.67 GPa, respectively. The optimized coefficients and exponents obtained by least-squares fitting of Eqn. 4 (shown as solid lines (Model 2) in Figure 7) with the experimental data are tabulated in Table 3. The value of βD_{eff} , which measures the effective diffusivity of adatoms, is estimated to 47.6 nm²/s at $V_s = \text{FP}$. With applied substrate bias [$V_s = -20$ V to -40 V], βD_{eff} increases by a factor of at least two compared to FP. TiN films deposited with $V_s = -60$ to -100 V, βD_{eff} is smaller compared to lower V_s , but slightly increases with increase in $|V_s|$. The value of l , which measures the surface to the depth of defect generated by the energetics particle bombardments as well as the region of grain boundary densification increases from 0.21 nm (at $V_s = \text{FP}$) to ~ 0.7 nm (at $V_s = -100$ V). The least-squares fitted value of A, B, and D_i is tabulated in Table 3, in which, D_i is the diffusivity of defects created in the bulk of coatings that diffused to the surface. The best fitted values of D_i have a non-linear dependence to V_s and are 72.9 , 23.7 , 37.3 , 75.1 , 74.8 , and 59.5 nm²/s at $V_s = \text{FP}$, -20 , -40 , -60 , -80 , and -100 V, respectively.

Table 3 Least squares optimized pre-factors and exponents obtained by fitting the evolution of stress ($\langle \sigma_{111} \rangle$) vs. t_f in $\text{Al}_x\text{Ti}_{1-x}\text{N}$ with Eqn. 4 (Model 2).

V_s (V)	βD_{eff} (nm ² /s)				l (nm)				A (GPa)				B (GPa)				D_i (nm ² /s)			
	$x=0.0$	$x=0.2$	$x=0.5$	$x=0.6$	$x=0.0$	$x=0.2$	$x=0.5$	$x=0.6$	$x=0.0$	$x=0.2$	$x=0.5$	$x=0.6$	$x=0.0$	$x=0.2$	$x=0.5$	$x=0.6$	$x=0.0$	$x=0.2$	$x=0.5$	$x=0.6$
FP	47.6	81.4	87.5	50.1	0.21	0.43	0.30	0.30	-122.4	-25.9	-27.2	-12.0	-82.1	-27.8	-20.7	0.0	72.9	49.9	92.3	\emptyset
-20	143.9	201.0	147.6	70.2	0.30	0.46	0.44	0.56	-50.5	-48.8	-49.2	-31.6	-96.4	-35.0	-29.9	-20.1	23.7	57.5	49.7	89.9
-40	111.3	209.9	240.1	99.7	0.56	0.75	0.56	0.70	-82.9	-48.3	-60.7	-37.7	-118.1	-67.6	-49.5	-29.4	37.3	68.1	52.0	74.8
-60	60.0	76.6	42.6	194.75	0.76	0.80	-0.68	0.80	-149.9	-43.1	-149.8	-51.5	-45.0	-145.7	-65.1	-78.5	75.1	68.4	75.0	87.6
-80	66.6	\emptyset	\emptyset	\emptyset	0.50	\emptyset	\emptyset	\emptyset	-134.9	\emptyset	\emptyset	\emptyset	-50.5	\emptyset	\emptyset	\emptyset	74.8	\emptyset	\emptyset	\emptyset
-100	75.4	\emptyset	\emptyset	\emptyset	0.67	\emptyset	\emptyset	\emptyset	-68.2	\emptyset	\emptyset	\emptyset	-47.2	\emptyset	\emptyset	\emptyset	59.5	\emptyset	\emptyset	\emptyset

B. Aluminium (25 at. %) titanium nitride ($\text{Al}_{0.25}\text{Ti}_{0.75}\text{N}$)

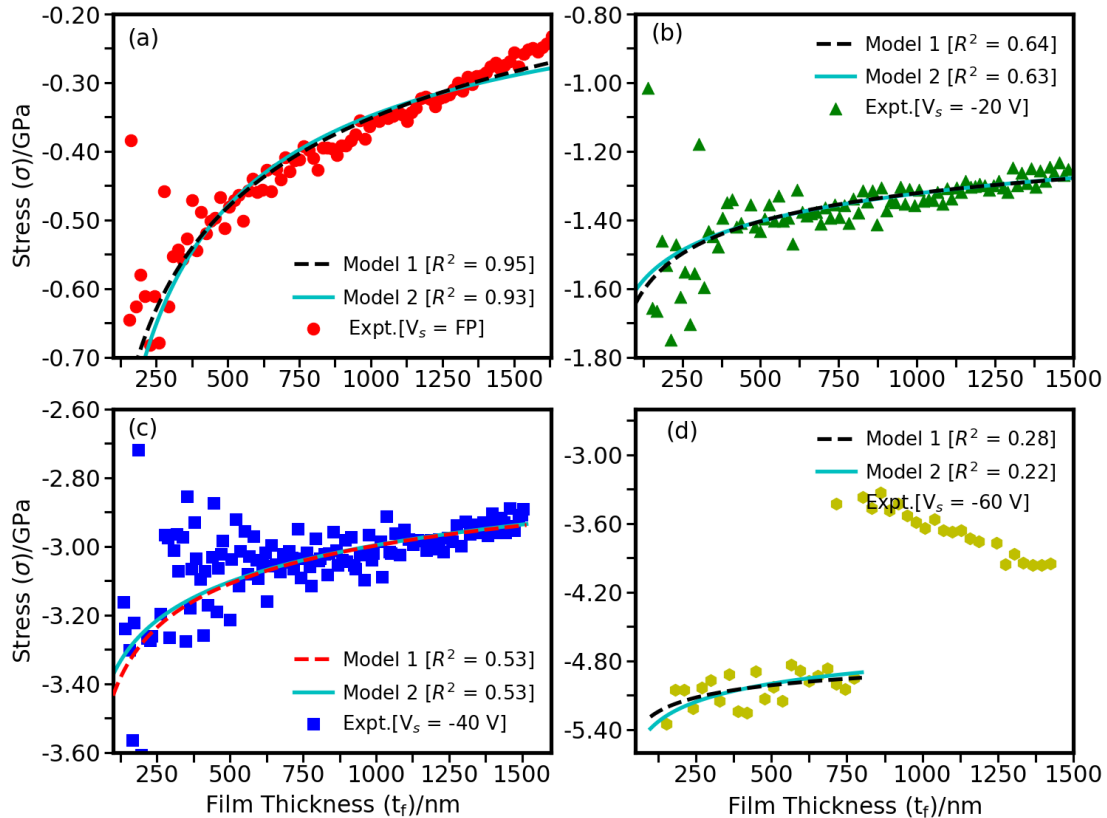


Figure 8 is the biaxial stress ($\langle\sigma_{111}\rangle$) evolution of $Al_{0.25}Ti_{0.75}N$ on Si (100) substrate at different substrate bias voltages V_s ; at floating potential (a), -20 V (b), -40 V (c), and -60 V (d). Experimentally obtained data are fitted with a power law (Model-1, dashed line) and a kinetic model (Model-2, solid lines) as discussed in section II.

The evolutions of σ vs t_f in $Al_{0.25}Ti_{0.75}N$ coatings at different V_s [FP, -20, -40, and -60 V] are shown in Figure 8. The IP-strain and IP interplanar spacing of $Al_{0.25}Ti_{0.75}N$ as a function of t_f are provided in Figure S-12 of SI. At $t_f \approx 250$ nm, the σ is approximately -0.7, -1.6, -3.2, and -5.1 GPa for coatings deposited with $V_s =$ FP, -20, -40, and -60 V, respectively. For coatings deposited with the $V_s =$ FP, -20, and -40 V, σ reduces with the increase in t_f . At the end of their deposition, the σ is estimated to -0.2, -1.2, and -2.9 GPa at $V_s =$ FP, -20, and -40 V, respectively, which suggests the increase in compressive stresses in the coating with -ve substrate bias. Similar to TiN, $Al_{0.25}Ti_{0.75}N$ coatings deposited with $V_s =$ -20 and -40 V, the value of σ is bit widespread. Unlike a smooth σ evolution of previously discussed TiN coatings, $Al_{0.25}Ti_{0.75}N$ with a V_s of -60 V shows a discontinuity in it at $t_f \approx 770$ nm, and σ changes from -4.94 GPa to -3.33 GPa (see Figure 8(d)). In the thickness region of $t_f \geq 770$ nm, σ vs. t_f is fitted with Eqn. 7, where $\sigma_{0,c}$ and γ are obtained as -4.28 GPa, -2.52 GPa nm $^\gamma$ and 0.2 respectively. The least-squared fitted value of σ_0 and c from Eqn. 3 are tabulated in Table 2. A consistent increase in absolute value of σ_0 with increase in V_s is noticed (see Table 2). The γ remain constant at 0.2 in all these three coatings (see Table 2).

Least-squares fitting of σ vs. t_f with Eqn. 4, with a fixed $\sigma_c = -0.02$ GPa and $\sigma_{T,0} = 0.85$ GPa at $L_0 = 100$ nm, revealed that at $V_s =$ FP, βD_{eff} is 81.4 nm $^2/s$ and increases more than two-fold upon substrate bias ($V_s =$ -20 and -40 V, see Table 3). Like TiN, in $Al_{0.25}Ti_{0.75}N$, the l increases from 0.43 nm to 0.75 nm with an increase in V_s from FP to -40 V (see Table 3). By varying V_s , the values of A changed from -25.9 to -43.1, while B increased from -27.8 GPa to -145.7 GPa, as V_s increases from FP to -40 V (see Table 3). The D_i also increases with an increase in V_s and changes from 48.9 to 68.4 nm $^2/s$, as V_s changes from FP to -40 V (see Table 3). As mentioned previously $Al_{0.25}Ti_{0.75}N$ coating deposited with $V_s =$ -60 V shows an abrupt change in stress at $t_f \approx 770$ nm, we analysed the stress evolution of the coating prior to this discontinuity. Least-squared fitting of σ vs. t_f in the given region of the coating revealed a relatively smaller βD_{eff} (≈ 76.6 nm $^2/s$) than that of other samples deposited with V_s of -20 and -40 V (see Table 3).

C. Aluminium (50 at. %) titanium nitride ($Al_{0.50}Ti_{0.50}N$)

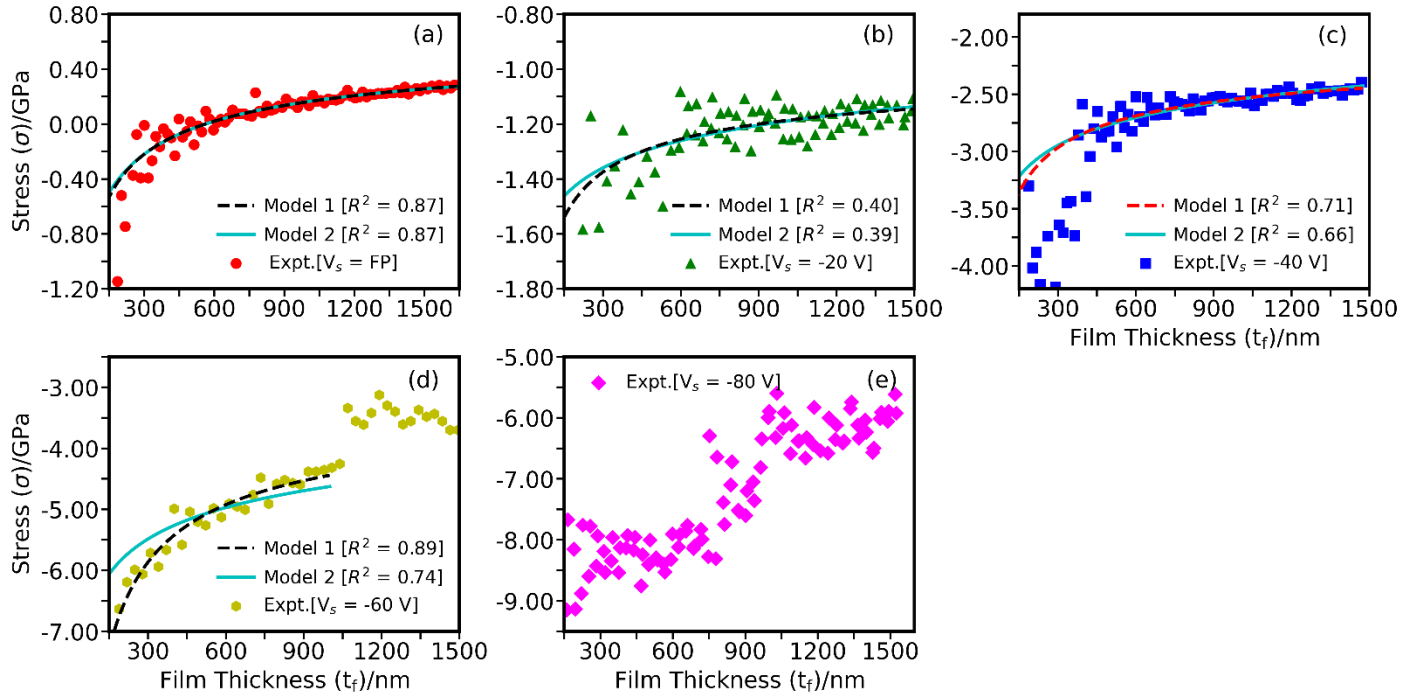


Figure 9 is the biaxial stress ($\langle\sigma_{111}\rangle$) evolution of $Al_{0.50}Ti_{0.50}N$ on Si (100) substrate at different substrate bias voltages V_s ; at floating potential (a), -20 V (b), -40 V (c), -60 V (d), and -80 V (e). Experimentally obtained data are fitted with a power law (Model 1, dashed line) and a kinetic model (Model 2, solid lines) as discussed in section II.

Unlike TiN and $\text{Al}_{0.25}\text{Ti}_{0.75}\text{N}$, $\text{Al}_{0.50}\text{Ti}_{0.50}\text{N}$ coating deposited with $V_s = \text{FP}$ shows average tensile stress in the coating beyond $t_f \gtrsim 600$ nm, while between $t_f \approx 185$ nm to 600 nm σ remains compressive (see Figure 9 (a)). At $t_f = 185$ nm, the estimated σ is -0.5 GPa, while σ shows a tensile nature and it reaches to 0.3 GPa at $t_f = 1640$ nm. With negative potential V_s , σ is compressive throughout t_f . The $\text{Al}_{0.50}\text{Ti}_{0.50}\text{N}$ coating deposited at $V_s = -20$ V shows a relatively weak evolution of σ (see Figure 9 (b)). At $t_f \approx 250$ nm, σ is estimated to ≈ -1.4 GPa, while σ converges to -1.1 GPa at $t_f \approx 1545$ nm. For the coating deposited with $V_s = -40$ V, we find a very strong stress relaxation between $t_f \approx 180$ -380 nm (see Figure 9 (c)). At $t_f \approx 180$ nm, estimated σ is -4.0 GPa, while at $t_f \approx 380$ nm σ is lowered down to -2.8 GPa. Similar to $\text{Al}_{0.25}\text{Ti}_{0.75}\text{N}$ coating deposited at $V_s = -60$ V, there is a discontinuity in σ vs. t_f of $\text{Al}_{0.50}\text{Ti}_{0.50}\text{N}$ coating at the same V_s . At $t_f \approx 950$ -1000 nm, the σ changes from -4.1 GPa to -3.3 GPa (see Figure 9 (d)). In this coating the estimated σ at $t_f \approx 180$ nm, is -6.5 GPa, while at $t_f \approx 950$ nm it is -4.2 GPa. $\text{Al}_{0.50}\text{Ti}_{0.50}\text{N}$ coating deposited at $V_s = -80$ V shows almost a constant σ of -8.2 GPa for $170 \text{ nm} \lesssim t_f \lesssim 745$ nm (see Figure 9 (e)). Beyond $t_f \gtrsim 745$ nm, an abrupt change in σ vs. t_f is observed. The σ evolution is fitted with Eqn. 3, and the coefficients and exponent are tabulated in Table 2. It is quite clear that the magnitude of converged stress σ_0 , as well as γ , increases with an increase in V_s .

Fitting of the kinetic model, Eqn. 4, to gain the evolution of σ , with $\sigma_c = -0.02$ GPa and $\sigma_{T,0} = 0.85$ GPa at $L_0 = 100$ nm, revealed the two to three fold increase in βD_{eff} value upon $V_s = -20$ and -40 V compared to $V_s = \text{FP}$ (see Table 3). Fitting of Eqn. 4 to σ vs. t_f , $200 \text{ nm} \lesssim t_f \lesssim 920$ nm, of $\text{Al}_{0.50}\text{Ti}_{0.50}\text{N}$ with $V_s = -60$ V, revealed βD_{eff} to be much smaller than the coating deposited with $V_s = \text{FP}$ (see Table 3). The value of l increases consistently from 0.30 nm to 0.68 nm with an increase in V_s from FP to -60 V. The optimized A [and B] are tabulated in Table 3, where a consistent increase in magnitude of A and B is seen with increase in $|V_s|$. The best fitting of D_i is obtained as 92.3, 49.7, 52.0, and 75.0 nm^2/s for $V_s = \text{FP}$, -20 V, -40 V, and -60 V, respectively (see Table 3).

D. Aluminium (67 at. %) titanium nitride ($\text{Al}_{0.67}\text{Ti}_{0.33}\text{N}$)

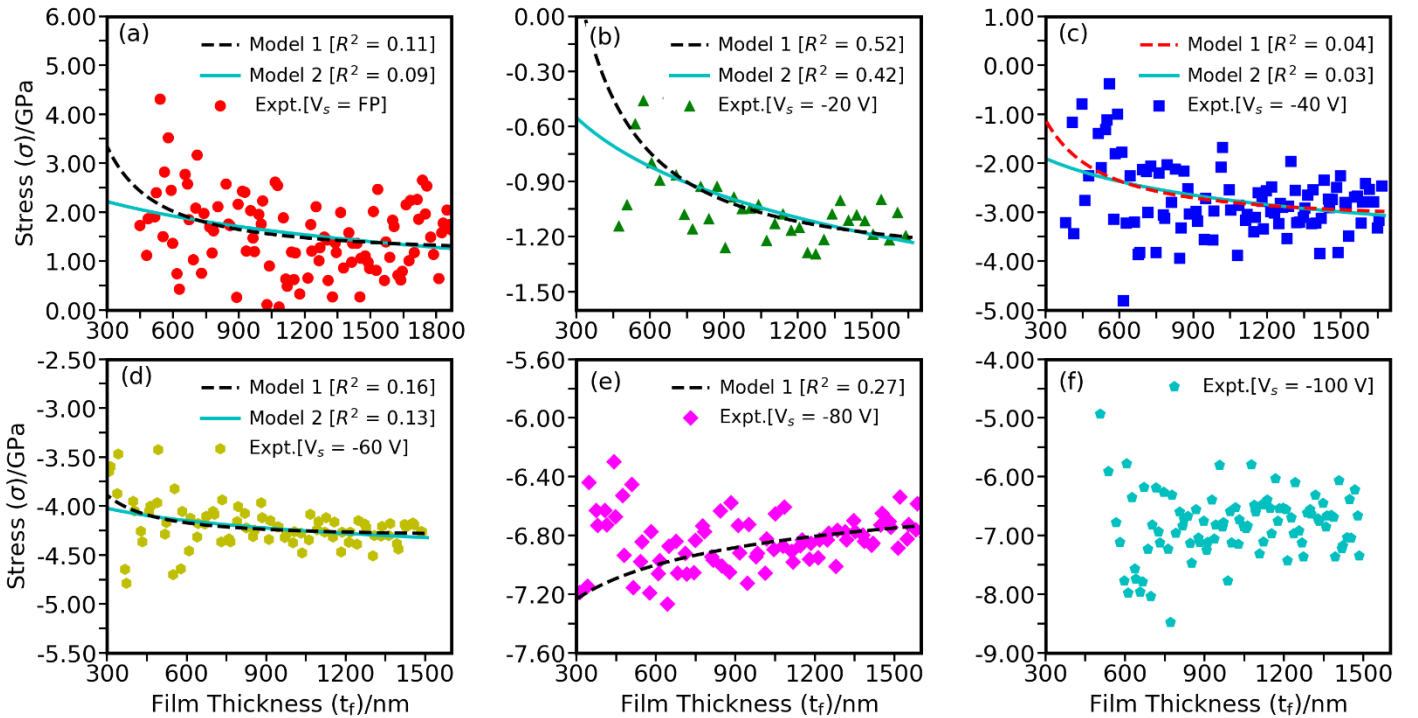


Figure 10 is the biaxial stress ($\langle \sigma_{111} \rangle$) evolution of $\text{Al}_{0.67}\text{Ti}_{0.33}\text{N}$ on Si (100) substrate at different substrate bias voltages V_s ; at floating potential (a), -20 V (b), -40 V (c), -60 V (d), -80 V (e), and -100 V (f). Experimentally obtained data are fitted with a power law (Model 1, dashed line) and a kinetic model (Model 2, solid lines) as discussed in section II.

Unlike $\text{Al}_x\text{Ti}_{1-x}\text{N}$: $x \leq 0.5$, a wider distribution of σ values are observed in $\text{Al}_{0.67}\text{Ti}_{0.33}\text{N}$ coatings (see Figure 10). The $\text{Al}_{0.67}\text{Ti}_{0.33}\text{N}$ coating deposited with $V_s = \text{FP}$ shows a net tensile stress with very high values of stress distribution within the recorded t_f ($300 \text{ nm} \lesssim t_f \lesssim 1870$ nm) with a mean σ of 1.6 GPa. With an increase in t_f , a reduction in the amplitude of tensile stress is noticeable (see Figure 10 (a)). The $\text{Al}_{0.67}\text{Ti}_{0.33}\text{N}$ coating with $V_s = -20$ V a net compressive stress is estimated and the magnitude of compressive

stress increases with an increase in t_f (see Figure 10 (b)). A similar σ evolution is observed in $\text{Al}_{0.67}\text{Ti}_{0.33}\text{N}$ coatings deposited with $V_s = -40$ and -60 V (see Figure 10 (b-c)). The average σ recorded with $\text{Al}_{0.67}\text{Ti}_{0.33}\text{N}$ coating with $V_s = -40$ V is ≈ -3.9 GPa. With $V_s = -60$ V, the evolution of σ is relatively better resolved than that of other $\text{Al}_{0.67}\text{Ti}_{0.33}\text{N}$ coatings (see Figure 10 (d)), and σ increases with an increase in t_f . At $t_f \approx 300$ nm, the average σ is assessed to be ≈ -3.9 GPa, while σ is ≈ -4.2 GPa at $t_f \approx 1615$ nm. The σ vs. t_f in $\text{Al}_{0.67}\text{Ti}_{0.33}\text{N}$ coating with $V_s = -80$ V is a bit different from that of other coatings. It appears that when t_f in the range of 300 to 600 nm, the σ is increased from -6.4 GPa to -6.9 GPa (see Figure 10 (e)). Beyond $t_f \approx 600$ nm, σ consistently decreases with the increase in t_f . The $\text{Al}_{0.67}\text{Ti}_{0.33}\text{N}$ coating deposited with a $V_s = -100$ V, the average σ remains around -6.8 GPa throughout the t_f (i.e., $600 \text{ nm} < t_f < 1502 \text{ nm}$).

To quantify the evolution of σ with t_f , experimentally determined data are fitted with Eqn. 3 as Model 1 in Figure 10. The least-squares optimized coefficients and exponents of the power-law are tabulated in Table 2. The magnitude of σ_0 increases consistently with the increase in V_s and changes from tensile to compressive as V_s changes from FP to $[-20, -100]$ V (see Table 2). Unlike $\text{Al}_x\text{Ti}_{1-x}\text{N}$: $x \leq 0.5$, the least-squares optimized values of c obtained for $\text{Al}_{0.67}\text{Ti}_{0.33}\text{N}$ are positive and remain fixed at 3474.1 GPa nm^γ with $\gamma = 1.29, 1.35, 1.35,$ and 1.58 for coatings deposited with $V_s = \text{FP}, -20 \text{ V}, -40 \text{ V},$ and -60 V , respectively. As mentioned previously, the evolution of σ in $\text{Al}_{0.67}\text{Ti}_{0.33}\text{N}$ coating deposited with $V_s = -80$ V is different, and the optimized $\sigma_0, c,$ and γ for the coating are -5.8 GPa, -6.1 GPa nm^γ , and 0.25 respectively (see Figure 10 (e) and Table 2).

It is to note that the estimated D_{111}^{IP} of $\text{Al}_{0.67}\text{Ti}_{0.33}\text{N}$ coatings are almost constant over t_f (see Figure 6 (d)). Thus, in fitting Eqn. 4 to model the evolution of σ in $\text{Al}_{0.67}\text{Ti}_{0.33}\text{N}$ we used $D_{111}^{\psi \in [45-55]^\circ}$ as $L(t_f)$ (see Figure S-9 (d) of SI and Eqn. 4). The least squared optimized fitting parameters from Eqn. 4 are tabulated in Table 3. Note that we have fixed $\sigma_C = -0.02$ GPa and best fitted value of $\sigma_{T,0}$ is 2.5 GPa at $L_0 = 100$ nm. The optimized value βD_{eff} ($50.1 \text{ nm}^2/\text{s}$) for $V_s = \text{FP}$ and it increases with increase in V_s (see Table 3). There is a consistent increase in value of l with an increase in V_s and increases from 0.30 nm [$V_s = \text{FP}$] to 0.8 nm [$V_s = -60 \text{ V}$]. Coating deposited with $V_s = \text{FP}$, the optimized A is -12.0 GPa, while B is very close to 0. The optimized magnitude of A [and B] consistently increases with increase in $|V_s|$. The best fitted D_j is obtained as $89.9, 74.8,$ and $87.6 \text{ nm}^2/\text{s}$ for $V_s = -20, -40,$ and -60 V , respectively.

V. DISCUSSION

Mechanism of formation of texture or preferred orientation of crystal planes in TMNs polycrystalline films are intensely debated in the literature. Broadly four different mechanisms are suggested: (i) minimization of overall energy [strain energy density, stopping energy, and surface free energy], (ii) anisotropic ion channelling along different crystallographic orientations, (iii) ratio of N to transition metals (TMs) at the surface of the substrate, and (iv) mobility of the impinging atoms on the surface of the growing films [44,58,59]. Rafaja *et al.* [60] further suggested that preferred orientations can be influenced by the experimental geometry too. Hultman *et al.* argued that because of the higher mobility of Ti-adatoms on on c-100 surface than c-111 surface [61] at pre-coalescence stage of islands, Ti adatoms have a higher chance of moving off c-001 faceted islands compared to c-111 faceted islands leading to low growth rate of c-001 faceted islands. But once the islands are coalesced, the effect is reversed, i.e., Ti adatoms will have more time to reside on c-111 surfaces than c-001 surfaces, thus the Ti adatoms capturing probability on c-111 surface is higher than on c-001 surface. Thus, as deposition proceeds c-111 oriented grains grow faster than c-001 oriented grains in a competitive growth mode that leads to c-111 preferred orientations of the films. This explains quite adequately the acquired texture from XRD patterns of TiN, $\text{Al}_{0.25}\text{Ti}_{0.75}\text{N}$, and $\text{Al}_{0.50}\text{Ti}_{0.50}\text{N}$ coatings deposited with $V_s = \text{FP}$, where c-111 is the preferred orientation.

Change in the texture orientation upon application of substrate bias voltage has been intensely debated in the literature. Based on first-principles analysis, Gall *et al.* [62] showed that in presence of lower atomic N concentration, the diffusion length of Ti adatoms on c-001 surfaces are comparatively higher than on c-111 surfaces. While at higher atomic N environment, c-200 surfaces will be covered with TiN_x like clusters, which results into a substantial drop of diffusion length of adatoms. In such growth conditions the preferential growth of c-200 grains take place. This partly explains the preferential orientation of our deposited TiN films with substrate bias, $|V_s| \geq 20$ V, where intensity of diffracted c-200 peak along the GD increases with an increase in V_s . While it is quite evident that in TiN, c-111 peak is always predominant along the GD irrespective of V_s , a careful visualization of XRD pattern (see Figure 1) reveals that the intensity of c-200 patterns is very strong close to the GD, but tilted $\approx 18^\circ/22^\circ$ away for coatings deposited with $V_s = -20, -40,$ and -60 V . We suspect such inclined texture of c-200 oriented grains is due to the geometry of the deposition process, where the incidence angle of the arc evaporated ions is at an angle of 35° to the direction substrate normal [63]. Furthermore, the return of c-111 texture from c-200 texture with higher V_s [$V_s = -80 \text{ V}$ and -100 V] could be the consequence of the recrystallization of c-200 orientated grains in to c-111 oriented grains as a consequent of secondary nucleation [64]. Schell *et al.* suggest that different

kinds of defects drive the recrystallization process [65], which agrees with the fact that higher substrate bias causes an increase in incident ion energy that can lead to the formation of high densities of surface defects as well as defects in the bulk.

Kinetics of adatoms in Al incorporated TiN is thoroughly investigated by Hultmann et al. [61] using first-principles calculations. They suggested that Al adatoms have higher mobility on TiN(001) than on TiN(111) surfaces. However, because of a lower diffusion activation barrier of Al in TiN(111) than that of Ti limits the kinetic advantage of Al adatoms in development of c-111 texture. The authors argued that incorporation of Al in the TiN(001) surface creates a trap state for Ti near substitutional Al_{Ti} site and Al at Al_{Ti} site of TiN(111). They proposed that in presence of Al_{Ti} trap states the chemical potential advantage for formation of c-111 texture reduces. This agrees well with our observation for Al_{0.25}Ti_{0.75}N and Al_{0.50}Ti_{0.50}N coatings. For a given V_s, diffraction intensity from c-200 crystal plane is higher for Al_{0.50}Ti_{0.50}N than Al_{0.25}Ti_{0.75}N coatings. The continuous reduction in the tilt angle of intense diffraction spots of c-200 crystal planes from the GD with increase in V_s for TiN, Al_{0.25}Ti_{0.75}N and Al_{0.50}Ti_{0.50}N suggests that the kinetics of adatoms can overcome the geometry-introduced constraints in the microstructure evolution.

Presence of both cubic and hexagonal phases in Al_{0.67}Ti_{0.33}N deposited with substrate bias V_s = FP, -20, -40, and -60 V bias are in good agreement with the results of theoretical estimations[36,37], where for x ≈ 0.64 -74 both hexagonal and cubic phases can be formed. Daniel *et al.* [66] demonstrated that beyond V_s of -50 V, hexagonal phases become the minority and eventually vanish at further higher voltages, which agrees with our experimental observations. The preferred orientation of h-10 $\bar{1}0$ crystal planes of Al_{0.67}Ti_{0.33}N deposited at V_s = FP can be understood through considering texture formation in PVD coated polycrystalline h-AlN [67]. Jin *et al.*[67] suggested that in h-AlN there are two types of Al-N bonds available, namely B₁ and B₂. While bond B₁ is more covalent, B₂ is more ionic [67] and the bond energy of type-B₂ is smaller than that of B₁, thus bond type B₂ is relatively easy to break. On the h-10 $\bar{1}0$ surfaces of h-AlN, only B₁ type bonds, while on h-0001 surfaces both B₁ and B₂ types are populated. Thus, with high energetics ion beams, the probability of survival of bond type B₁ in AlN is higher than that of B₂ type, indicating h-0001 faceted grains grow faster with high substrate bias. The first principles estimated surface free energy of h-AlN [68] suggests that the h-10 $\bar{1}0$ surface has lower surface free energy than that of h-0001 surfaces, suggesting with non-energetics ion beams the h-10 $\bar{1}0$ surface will grow along the GD. Cheng *et al.* [69] also suggested that for the development of closed packed surface planes (i.e. h-0001 surfaces) adatoms need to stay a longer time at the surface than that of loosely packed surface (i.e. h-10 $\bar{1}0$). The preferred orientation of h-10 $\bar{1}0$ along the GD in Al_{0.67}Ti_{0.33}N coating deposited at V_s = FP agrees with predictions of three different mechanisms as discussed above. With increase in |V_s|, together with breaking of B₂ type bonds along with the higher diffusivity of adatoms causes preferred orientation of h-0002 along the GD. The orientation of c-111 and c-200 crystal planes of c-Al_{0.67}Ti_{0.33}N is a bit different than that of Al_xTi_{1-x}N; x ≤ 0.5. The intense spot of c-111 always remains fixed at an angle of 42° to the GD, while for |V_s| ≥ 60 V, the intense spot in c-200 Debye-Scherrer rings tilted away from 16° to 24° from the GD.

The correlation between **k** and **n**, obtained by fitting the evolution of crystallite size, is estimated based on the Kendall rank correlation test [70]. The estimated *p*-values of **k** and **n** for individual compositions are .021, .083, .017, and .055 (.007) for TiN, Al_{0.25}Ti_{0.75}N, Al_{0.50}Ti_{0.50}N, Al_{0.67}Ti_{0.33}N (Al_{0.67}Ti_{0.33}N: ψ ∈ [45°-55°]), respectively. This suggests that a significant correlation between estimated **k** and **n** exists. We also checked Pearson's correlation between **k** and **n**, where the magnitude of correlation coefficient is higher than 0.88, hinting to a strong linear correlation, indeed we find that there is a strong linear correlation between log(**k**) and **n** (see Figure S-9 of SI) [71]. In such case, Depla *et al.*[71] proposed that the power-law [Eqn. 2] need modifications, and the modified version of the power-law is given by;

$$\frac{D_{hkl}}{D_0} = \left(\frac{t_f}{t_0}\right)^n \quad (5)$$

where D₀ and t₀ are two constants. Fitting of D₁₁₁^{IP} vs. t_f with Eqn. 5 revealed that the D₀ and t₀ values for all Al_xTi_{1-x}N are very close to each other, and the mean values are 13.43 ± 3.60 nm, and 12.41 ± 2.40 nm. Fitted D₀ and t₀ for all Al_xTi_{1-x}N coatings at various V_s are further tabulated in section SI. IV of SI. The optimized **n** values are tabulated in Table 4. The value t₀ approximates very close to the mean film thickness for continuous film formation [71–73]. Thus, here we argue that the critical thickness for which the arc evaporated Al_xTi_{1-x}N transitions from discrete islands to continuous films happens to be close 12.41 ± 2.40 nm.

The homologous temperature, defined as the ratio of substrate temperature (~ 450 °C [~723 K]) and melting temperature of materials (~2949 °C [~ 3222 K] [74], of our deposited films are close to 0.22. At such low homologous temperature a substantially lower value of mean growth exponent, **n** < 0.35, is often observed[71] in agreement with our estimation. The **n** [from Eqn. 2 and Eqn. 5] is higher with films deposited with V_s = FP and lays between ≈ 0.25 to 0.4. With V_s, **n** reduces to ≈ 0.15 to ≈ 0.18 at -20 V and further increases to ≈ 0.23 at V_s = -100 V (see Table 4). This “U” shape of **n** vs V_s suggests a competitive growth mechanism, possibly a competition between nucleation rates caused by energetics ions, creation of defects, and diffusion of energetics adatoms [75]. A consistent increase in average grain size, D₁₁₁^{IP}, with an increase in film thickness is a consequence of grain coarsening,

coalescence of smaller grains to larger grains, and grain growth below the surface of growing films, as the film thickness/growth duration increases [76]. The *nanocrystalline*-like surface morphologies (see Figure 3(p-u) and Figure 5(a-1, b-1, and c-1)) and evolution of grain size (see Figure 6 (d) and Figure S-9 (d) of SI) of $\text{Al}_{0.67}\text{Ti}_{0.33}\text{N}$ coatings suggests that a frequent re-nucleation of grains occurs during the entire growth durations. Our TEM analysis indicates that formation of hexagonal phases around the grain boundaries is the reason behind the stagnation and, hence, the frequent re-nucleation of grains.

Table 4: Optimized exponent n as obtained by fitting Eqn. 5 with the D_{111}^{IP} vs. t_f of $\text{Al}_x\text{Ti}_{1-x}\text{N}$ coatings on Si (100) substrate.

V_s (V)	n (TiN)	n ($\text{Al}_{0.25}\text{Ti}_{0.75}\text{N}$)	n ($\text{Al}_{0.50}\text{Ti}_{0.50}\text{N}$)	n ($\text{Al}_{0.67}\text{Ti}_{0.33}\text{N}$)
FP	0.25	0.33	0.40	-0.09
-20	0.15	0.12	0.09	0.01
-40	0.18	0.14	0.18	-0.01
-60	0.19	0.14	0.15	0.04
-80	0.23	-	0.15	0.09
-100	0.23	-	-	-0.10

The generation of compressive stress in PVD coated thin films is often observed. Among the many mechanisms, the insertion of atoms into the grain boundary has been gaining more credibility [56,77]. However, in the deposition of coatings with high energetics vapour flux, stress can be caused by additional factors, too. A comprehensive model proposed by Chason *et al.* [56] includes such factors [e.g., boundary coalescence, formation of the new grain boundaries, and their densification and creation of defects in bulk of films].

In general, it is seen here that the βD_{eff} , which is a measure of effective diffusivity, increases with increase in V_s . However, in our TiN coatings βD_{eff} shows a “U” type behaviour with increase in V_s . This behaviour coincides with the “U” type character of the evolution of the texture intensity ratio I_{c-200}/I_{c-111} (see Figure S-5 of SI). The βD_{eff} in $\text{Al}_{0.25}\text{Ti}_{0.75}\text{N}$, and $\text{Al}_{0.50}\text{Ti}_{0.50}\text{N}$ coatings deposited with $V_s = \text{FP}$ is substantially lower than for coatings deposited with applied negative V_s [except for coatings with cohesive failure is seen]. This applied V_s influences diffusivity of adatoms, and it increases with an increase in ion energies. This agrees with the fact that with increase in $|V_s|$ wider nanocolumnar dense coatings are seen. The βD_{eff} of TiN, $\text{Al}_{0.25}\text{Ti}_{0.75}\text{N}$, and $\text{Al}_{0.50}\text{Ti}_{0.50}\text{N}$ is within the range of 47-210 nm^2/s , much higher than that reported for different metals and TiN thin films deposited by magnetron sputtering ($\beta D_{\text{eff}} = 0.12 \text{ nm}^2/\text{s}$ for TiN) [30,78]. For “non-energetics” electrodeposited Ni and Cu samples the reported absolute values of βD_{eff} varied quite differently from that mentioned earlier. Chason *et al.* [79–81] reported βD_{eff} to be around 174 nm^2/s to 1761 nm^2/s in the same order as our predictions. The fitted parameters A and B, for arc evaporated TiN, that we obtained from least-squares fitting, are in agreement with different materials that are discussed in the literature [30,56,78]. The value of l increases with an increase in V_s further agreeing that with an increase in kinetic energy, ions can penetrate more into the bulk of thin films from the surfaces. The obtained order of l agrees with the ranges of the value predicted [30]. We find that the evolution of A and B with V_s is not necessarily linear. In TiN coatings, the magnitude of final stress level at the end of deposition is of the “U” type with the V_s . This suggests that the A and B in the kinetic model may have a dependence on the texture/microstructure of the polycrystalline thin films and do not necessarily increase with an increase in the ion energies alone. Interestingly, the evolution of A and B obtained from the least square fitting of stress evolution of $\text{Al}_{0.25}\text{Ti}_{0.75}\text{N}$ and $\text{Al}_{0.50}\text{Ti}_{0.50}\text{N}$ with different V_s are a bit different from TiN. In the case of $\text{Al}_{0.25}\text{Ti}_{0.75}\text{N}$, values of both A and B increases with an increase in V_s , except for $V_s = -60 \text{ V}$ where a small decrease in A is noticed .

No strong power-law type evolution of σ is observed in $\text{Al}_{0.50}\text{Ti}_{0.50}\text{N}$ deposited with $V_s = -80 \text{ V}$, suggesting high ion energies can create a large density of defects, including dislocations and twin boundaries [82,83], which can give rise to high stress state in the coating. At the same time high densities of surface defects can hinder the mobility of adatoms, which adds to the already high σ to the films. This hypothesis is further tested for $\text{Al}_{0.25}\text{Ti}_{0.75}\text{N}$ and $\text{Al}_{0.50}\text{Ti}_{0.50}\text{N}$ coatings deposited at $V_s = -60 \text{ V}$, where the cohesive failure of films is seen. The βD_{eff} values for both these coatings are substantially lower than for the coatings deposited at $V_s = -40 \text{ V}$ (see Table 3) suggesting low diffusivity of adatoms on surface may be one of the reasons for higher internal stress in the coating.

The estimated values of diffusivity of defects, D_i , generated in the bulk part of the materials are diverse in the literature. For sputter-deposited TiN, Mo, and Cu, the D_i is estimated, using the kinetic model as discussed in section III, around 9.87 nm^2/s , 0.28 nm^2/s and 5503.14 nm^2/s [30,56,78]. Through numerical simulations, Pasianot *et al.* [84] and Starikov *et al.* [85] predict the value of D_i , $\sim 1260 \text{ nm}^2/\text{s}$ and $10^{10} \text{ nm}^2/\text{s}$ respectively. Our predicted diffusivity D_i , with TiN, $\text{Al}_{0.25}\text{Ti}_{0.75}\text{N}$, and $\text{Al}_{0.50}\text{Ti}_{0.50}\text{N}$ are in the order of

$10^1\text{-}10^2 \text{ nm}^2/\text{s}$. At this stage, we do not find any correlation between the V_s and D_i . Since no reports are available regarding the estimation of D_i for arc evaporated coatings in the literature, we could not compare our estimates either. The cohesive failures in PVD coated films are well documented and are often attributed to high stress level, i.e., when the stress level is higher than the fracture toughness, the coating releases the excess strain energy through the formation of cracks in the coating [47].

The evolution of σ in $\text{Al}_{0.67}\text{Ti}_{0.33}\text{N}$ coatings is more scattered in comparison to $\text{Al}_x\text{Ti}_{1-x}\text{N}$; $x \leq 0.5$. This is a consequence of a larger stress distribution caused by finer grains, compositional fluctuations, and formation of multi-phase crystal structure etc. High tensile stress in $\text{Al}_{0.67}\text{Ti}_{0.33}\text{N}$ deposited at $V_s = \text{FP}$ is possibly the consequence of very small grain size (L) as tensile stress, σ_T , scales as $L^{-0.5}$. Through a detailed molecular dynamics simulation of bcc metals, Thompson *et al.* [86] proposed that stress evolution is also dependent on surface morphology. They found that when grains are well separated, and impinging energy of atoms is lower ($\sim 5 \text{ eV}$) the stress is tensile, and it scales with reduced contact area between the islands. Cross-sectional SEM and TEM suggest a “perpendicular edge” like structure, indicating that the surface morphology is the key behind this tensile stress. A flatter surface morphology in $\text{Al}_{0.67}\text{Ti}_{0.33}\text{N}$ coatings deposited with different V_s along with the mechanisms of Eqn. 4 is responsible for compressive stress. Unlike $\text{Al}_x\text{Ti}_{1-x}\text{N}$; $x \leq 0.5$, in $\text{Al}_{0.67}\text{Ti}_{0.33}\text{N}$ stress increases with increase in t_f ($V_s = -20, -40, \text{ and } -60 \text{ V}$). The least-squared fitted c for Model 1 is the same for $\text{Al}_{0.67}\text{Ti}_{0.33}\text{N}$ coatings for $V_s = \text{FP}, -20, -40, \text{ and } -60 \text{ V}$, which is probably the consequence of similar crystallite sizes ($D_{111}^{\text{IP}} \approx 8\text{-}12 \text{ nm}$). The origin of the unusually small, but finite decrease in σ with the increase in t_f in $\text{Al}_{0.67}\text{Ti}_{0.33}\text{N}$ coatings deposited with $V_s = -80 \text{ V}$ is unknown to us. We suggest such behaviour might have a pure microstructure origin or is the consequence of the formation of cubic phase crystal only. With $V_s = -100$, the estimated σ is almost constant, suggesting that formation of large densities of defects due to energetic ions are dictating the stress levels in the coatings. The fitted value of βD_{eff} increases with an increase in V_s from FP to -60 V suggesting the net diffusivity of adatoms increases despite frequent re-nucleation. The value of $A, B, \text{ and } l$ increases with an increase in V_s , which agrees with the suggestions made by Chason *et al.* [56]. The best-fitted value of B from the $\text{Al}_{0.67}\text{Ti}_{0.33}\text{N}$ coating deposited with $V_s = \text{FP}$ is obtained as 0, as at no t_f , σ is compressive. A value of $D_i \approx 75\text{-}90 \text{ nm}^2/\text{s}$ is noted. As already discussed earlier, there are no reports in the literature for which D_i values can be compared for arc evaporated films.

In short, an effective compressive stress relaxation in $\text{Al}_x\text{Ti}_{1-x}\text{N}$; $x \leq 0.5$ coatings with the increase in t_f is seen, and it is a consequence of the average increase in crystallite size (also grain size) at higher t_f . An accumulation of compressive stress is observed in $\text{Al}_{0.67}\text{Ti}_{0.33}\text{N}$, where a substantial hexagonal phase is recorded. In absence of hexagonal phases, a small but noticeable compressive stress relaxation is seen. Thus, here we argue that stress relaxation in $\text{Al}_x\text{Ti}_{1-x}\text{N}$ coatings with increase in film thickness is a combined effect of grain growth as well as the fraction of hexagonal phases in them.

Table 5: Critical stress (σ_{cr}), critical film thickness (h_{cr}), plain strain fracture toughness (K_{IC}), and elastically stored energy (G_s) obtained for $\text{Al}_{0.25}\text{Ti}_{0.75}\text{N}$ deposited with substrate bias (V_s) of -60 V , and $\text{Al}_{0.50}\text{Ti}_{0.50}\text{N}$ deposited with substrate bias (V_s) of -60 V , and -80 V .

Composition	V_s (V)	σ_{cr} (GPa)	h_{cr} (nm)	K_{IC} (MPa.m ^{1/2})	G_s (J/m ²)
Al_{0.25}Ti_{0.75}N	-60	-4.9 ± 0.10	770 ± 20	3.09 ± 0.05	23.5
Al_{0.50}Ti_{0.50}N	-60	-4.4 ± 0.15	950 ± 50	3.04 ± 0.12	23.8
Al_{0.50}Ti_{0.50}N	-80	-7.9 ± 0.18	745 ± 25	4.84 ± 0.12	55.9

As mentioned earlier, the cohesive failure of the coatings is attributed to a high-stress field in the coatings, and the critical stress at which it fails is characteristic of fracture toughness of the materials. In the thin film forms, it is difficult to estimate the fracture toughness due to their small size and unreliable methods. Huang *et al.* [47] developed a method by using stored internal energy. In that proposed method, many polycrystalline thin film coatings were deposited with varying thickness and residual stress (σ). The shortcoming of their work is the exact determination of the film thickness, at which the cracks form and propagate. This shortcoming can be overcome by *in-situ* measurements, such as utilized in the current work. Since from *in-situ* XRD data analysis, we can determine critical residual stress (σ_{cr}) and critical film thickness (h_{cr}) at which initiations and propagations of cracks occur [i.e., location of discontinuity in XRD peak intensity, crystallite size and stress evolution]. For thin films, Huang *et al.* [47] approximated the plain strain fracture toughness (K_{IC}) to elastically stored energy (G_s) and critical stress and h_{cr} by the relation given below.

$$K_{\text{IC}} = \frac{1}{\sqrt{2}} |\sigma_{\text{cr}}| \sqrt{h_{\text{cr}}} = \sqrt{\frac{E_{\text{hkl}} G_s}{(1 - \nu_{\text{hkl}}^2)}} \quad (6)$$

Utilizing the values of σ and t_f , at which discontinuity in stress and diffraction intensity evolution happens and using them as σ_{cr} and h_{cr} respectively in Eqn. (6), we estimate the K_{IC} and G_s for samples, where cohesive failure is seen. The values are tabulated in Table 5.

The estimated K_{IC} values closely agree with the estimate of Mayrhofer *et al.* ($K_{IC} = 2.7 \pm 0.3 \text{ MPa.m}^{1/2}$ for $\text{Al}_{0.60}\text{Ti}_{0.40}\text{N}$ [87] and $3.5 \pm 0.3 \text{ MPa.m}^{1/2}$ for $\text{Al}_{0.46}\text{Ti}_{0.54}\text{N}$ [88]). The K_{IC} estimated for $\text{Al}_{0.50}\text{Ti}_{0.50}\text{N}$ with $V_s = -80 \text{ V}$ is a bit higher. A relatively higher K_{IC} of $\text{Al}_{0.25}\text{Ti}_{0.75}\text{N}$ and $\text{Al}_{0.50}\text{Ti}_{0.50}\text{N}$ than that of TiN [47,89] agrees with the theoretical prediction of Abrikosov *et al.* [90].

VI. SUMMARY

In summary, we investigate the real-time evolution of stress and microstructure of aluminium titanium nitride ($\text{Al}_x\text{Ti}_{1-x}\text{N}$, $0.0 \leq x \leq 0.67$) thin films on Si (100) substrate during their deposition with a custom-designed cathodic arc deposition technique. The synchrotron-based 2-dimensional in-situ x-ray diffractograms of coatings are recorded during the depositions. The strain and biaxial stress are evaluated by utilizing $\sin^2\psi$ method, and their evolution with film thicknesses is analysed within a kinetic model. Line profile analysis is carried out to quantify the evolution of crystallite sizes and texture formation. Thorough ex-situ characterizations of the coatings were carried out using electron microscopies tools. The main conclusions derived from this work are as follows.

- While in coatings of $\text{Al}_x\text{Ti}_{1-x}\text{N}$: $x \leq 0.5$ long columnar morphologies are formed, where the domain size of nanocolumns and the density of coatings increase with an increase in substrate bias voltage. Owing to higher adatoms' effective diffusivity, $\text{Al}_{0.67}\text{Ti}_{0.33}\text{N}$ coatings have nanocrystalline-like surface morphology. The nanocrystalline-like surface morphology is driven by the re-nucleation of grains and is a consequence of the formation of mixed hexagonal and cubic phases.
- At lower energy of incoming ions (i.e., substrate at floating potential), 111 crystal planes of cubic phases of $\text{Al}_x\text{Ti}_{1-x}\text{N}$: $x \leq 0.5$ are preferentially oriented along the growth direction while in $\text{Al}_{0.67}\text{Ti}_{0.33}\text{N}$ coating 220 crystal planes of cubic phases and $10\bar{1}0$ and $11\bar{2}0$ crystal planes of hexagonal phases are oriented parallel to the interface of coatings and substrates. Irrespective of Al content in $\text{Al}_x\text{Ti}_{1-x}\text{N}$ coatings, an increase in ion energies drives 200 crystal planes of cubic phases to preferentially orient along/close the GD.
- A power law-like evolution of crystallites' dimension along the in-plane direction with film thickness is observed. While for $\text{Al}_x\text{Ti}_{1-x}\text{N}$: $x \leq 0.5$ coatings the exponent of the power is positive and lies between 0.15 and 0.4, the exponent for $\text{Al}_{0.67}\text{Ti}_{0.33}\text{N}$ is within the range of ± 0.1 . Analysis of the evolution of crystallite size vs. coating thickness revealed that in arc evaporated $\text{Al}_x\text{Ti}_{1-x}\text{N}$ coatings the critical thickness of transformation from discrete islands to continuous films is $12.41 \pm 2.40 \text{ nm}$.
- The biaxial stress in $\text{Al}_x\text{Ti}_{1-x}\text{N}$ coatings follows a power law-like behaviour with thickness of thin film. The converged value of stress in $\text{Al}_x\text{Ti}_{1-x}\text{N}$ coatings deposited at floating potential substrate bias is always tensile, while they are compressive with the negative substrate bias voltages. In all $\text{Al}_x\text{Ti}_{1-x}\text{N}$: $x \leq 0.5$ coatings a biaxial stress relaxation with increase in film thickness is observed, while in $\text{Al}_{0.67}\text{Ti}_{0.33}\text{N}$ coatings an increase in biaxial compressive stress with film thickness is observed. Kinetic modelling analysis suggests that upon a negative substrate bias a two-to-three-fold increase in effective diffusivity of adatoms occurs. The length ion induced densification of grain boundaries and to the depth at which defects are being created increases from 0.2-0.3 nm to 0.7-0.8 nm, as the substrate bias changes from the floating potential to -100 V .
- Based on their critical stress level at the critical film thickness before fracture, the estimated fracture toughness of $\text{Al}_{0.25}\text{Ti}_{0.75}\text{N}$ and $\text{Al}_{0.50}\text{Ti}_{0.50}\text{N}$ coatings are in the $3.09 \pm 0.1 \text{ MPa.m}^{1/2}$ and $[3.04 \pm 0.1, 4.84 \pm 0.13] \text{ MPa.m}^{1/2}$ respectively agreed well with estimation from other techniques reported in the literature.

Acknowledgements: All authors acknowledge DESY for beamtime under proposal I-20210060EC. We acknowledge financial support from the Swedish Research Council via the Röntgen Ångström Cluster (RÅC) Frame Program.

References

- [1] N.G. Dhere, R.G. Dhere, Thin-film photovoltaics, *J. Vac. Sci. & Technol. A Vacuum, Surfaces, Film.* 23 (2005) 1208–1214.
- [2] S. Wagner, Thin-film semiconductors—From exploration to application, *MRS Bull.* 43 (2018) 617–624.
- [3] Y. Li, F. Qian, J. Xiang, C.M. Lieber, Nanowire electronic and optoelectronic devices, *Mater. Today.* 9 (2006) 18–27. [https://doi.org/10.1016/S1369-7021\(06\)71650-9](https://doi.org/10.1016/S1369-7021(06)71650-9).

- [4] H.D. Espinosa, B.C. Prorok, M. Fischer, A methodology for determining mechanical properties of freestanding thin films and MEMS materials, *J. Mech. Phys. Solids*. 51 (2003) 47–67. [https://doi.org/10.1016/S0022-5096\(02\)00062-5](https://doi.org/10.1016/S0022-5096(02)00062-5).
- [5] H. Coufal, Photothermal spectroscopy using a pyroelectric thin-film detector, *Appl. Phys. Lett.* 44 (1984) 59–61.
- [6] C.W. Ahn, G. Amarsanaa, S.S. Won, S.A. Chae, D.S. Lee, I.W. Kim, Antiferroelectric thin-film capacitors with high energy-storage densities, low energy losses, and fast discharge times, *ACS Appl. Mater. & Interfaces*. 7 (2015) 26381–26386.
- [7] T.G. Bifano, H.T. Johnson, P. Bierden, R.K. Mali, Elimination of stress-induced curvature in thin-film structures, *J. Microelectromechanical Syst.* 11 (2002) 592–597.
- [8] M.R. Vaezi, S.K. Sadrnezhaad, L. Nikzad, Electrodeposition of Ni--SiC nano-composite coatings and evaluation of wear and corrosion resistance and electroplating characteristics, *Colloids Surfaces A Physicochem. Eng. Asp.* 315 (2008) 176–182.
- [9] E. Chason, P.R. Guduru, Tutorial: Understanding residual stress in polycrystalline thin films through real-time measurements and physical models, *J. Appl. Phys.* 119 (2016). <https://doi.org/10.1063/1.4949263>.
- [10] V.M. Marx, F. Toth, A. Wiesinger, J. Berger, C. Kirchlechner, M.J. Cordill, F.D. Fischer, F.G. Rammerstorfer, G. Dehm, The influence of a brittle Cr interlayer on the deformation behavior of thin Cu films on flexible substrates: Experiment and model, *Acta Mater.* 89 (2015) 278–289. <https://doi.org/10.1016/j.actamat.2015.01.047>.
- [11] M.W. Moon, J.W. Chung, K.R. Lee, K.H. Oh, R. Wang, A.G. Evans, An experimental study of the influence of imperfections on the buckling of compressed thin films, *Acta Mater.* 50 (2002) 1219–1227. [https://doi.org/10.1016/S1359-6454\(01\)00423-2](https://doi.org/10.1016/S1359-6454(01)00423-2).
- [12] C. Coupeau, Atomic force microscopy study of the morphological shape of thin film buckling, *Thin Solid Films*. 406 (2002) 190–194. [https://doi.org/10.1016/S0040-6090\(01\)01772-2](https://doi.org/10.1016/S0040-6090(01)01772-2).
- [13] R. Boijoux, G. Parry, J.Y. Faou, C. Coupeau, How soft substrates affect the buckling delamination of thin films through crack front sink-in, *Appl. Phys. Lett.* 110 (2017). <https://doi.org/10.1063/1.4979614>.
- [14] G.G. Stoney, The tension of metallic films deposited by electrolysis, *Proc. R. Soc. London. Ser. A, Contain. Pap. a Math. Phys. Character.* 82 (1909) 172–175.
- [15] Rosse, Bimetallic Mirrors Made by Electro-Depositions, *Nat.* 78 (1908) 366–367.
- [16] J.F. Meng, N.V.C. Shekar, J. V Badding, D.Y. Chung, M.G. Kanatzidis, Multifold enhancement of the thermoelectric figure of merit in p-type BaBiTe₃ by pressure tuning, *J. Appl. Phys.* 90 (2001) 2836–2839.
- [17] E. Bousquet, N.A. Spaldin, P. Ghosez, Strain-induced ferroelectricity in simple rocksalt binary oxides, *Phys. Rev. Lett.* 104 (2010) 37601.
- [18] F. Tasnádi, B. Alling, C. Höglund, G. Wingqvist, J. Birch, L. Hultman, I.A. Abrikosov, Origin of the anomalous piezoelectric response in wurtzite scxA11-xN alloys, *Phys. Rev. Lett.* 104 (2010) 1–4. <https://doi.org/10.1103/PhysRevLett.104.137601>.
- [19] M. El Kurdi, H. Bertin, E. Martincic, M. De Kersauson, G. Fishman, S. Sauvage, A. Bosseboeuf, P. Boucaud, Control of direct band gap emission of bulk germanium by mechanical tensile strain, *Appl. Phys. Lett.* 96 (2010) 41909.
- [20] Y.-C. Huang, S.-Y. Chang, C.-H. Chang, Effect of residual stresses on mechanical properties and interface adhesion strength of SiN thin films, *Thin Solid Films*. 517 (2009) 4857–4861.
- [21] P.H. Mayrhofer, C. Mitterer, J. Musil, Structure--property relationships in single-and dual-phase nanocrystalline hard coatings, *Surf. Coatings Technol.* 174 (2003) 725–731.
- [22] E. Aschauer, M. Bartosik, H. Bolvardi, M. Arndt, P. Polcik, A. Davydok, C. Krywka, H. Riedl, P.H. Mayrhofer, Strain and stress analyses on thermally annealed Ti-Al-N/Mo-Si-B multilayer coatings by synchrotron X-ray diffraction, *Surf. Coatings Technol.* 361 (2019) 364–370.
- [23] M. Hÿtch, F. Houdellier, F. Hüe, E. Snoeck, Nanoscale holographic interferometry for strain measurements in electronic devices, *Nature*. 453 (2008) 1086–1089. <https://doi.org/10.1038/nature07049>.
- [24] F. Ahmed, K. Bayerlein, S.M. Rosiwal, M. Göken, K. Durst, Stress evolution and cracking of crystalline diamond thin films on ductile titanium substrate: Analysis by micro-Raman spectroscopy and analytical modelling, *Acta Mater.* 59 (2011) 5422–5433. <https://doi.org/10.1016/j.actamat.2011.05.015>.
- [25] A.J. Wilkinson, G. Meaden, D.J. Dingley, High-resolution elastic strain measurement from electron backscatter diffraction

- patterns: New levels of sensitivity, *Ultramicroscopy*. 106 (2006) 307–313. <https://doi.org/10.1016/j.ultramic.2005.10.001>.
- [26] Z. Rao, S. Berman, P. Yang, D. Depla, E. Chason, Understanding residual stress in thin films: Analyzing wafer curvature measurements for Ag, Cu, Ni, Fe, Ti, and Cr with a kinetic model, *J. Appl. Phys.* 130 (2021) 135304.
- [27] T.R. Koenig, Z. Rao, E. Chason, G.J. Tucker, G.B. Thompson, The microstructural and stress evolution in sputter deposited Ni thin films, *Surf. Coatings Technol.* 412 (2021) 126973. <https://doi.org/10.1016/j.surfcoat.2021.126973>.
- [28] A.M. Engwall, Z. Rao, E. Chason, Residual stress in electrodeposited Cu thin films: Understanding the combined effects of growth rate and grain size, *J. Electrochem. Soc.* 164 (2017) D828.
- [29] D. Magnfält, A. Fillon, R.D. Boyd, U. Helmersson, K. Sarakinos, G. Abadias, Compressive intrinsic stress originates in the grain boundaries of dense refractory polycrystalline thin films, *J. Appl. Phys.* 119 (2016). <https://doi.org/10.1063/1.4941271>.
- [30] Z. Rao, E. Chason, Measurements and modeling of residual stress in sputtered TiN and ZrN: Dependence on growth rate and pressure, *Surf. Coatings Technol.* 404 (2020) 126462.
- [31] G. Abadias, P. Guerin, In situ stress evolution during magnetron sputtering of transition metal nitride thin films, *Appl. Phys. Lett.* 93 (2008) 111908.
- [32] G. Abadias, L.E. Koutsokeras, P. Guerin, P. Patsalas, Stress evolution in magnetron sputtered Ti--Zr--N and Ti--Ta--N films studied by in situ wafer curvature: role of energetic particles, *Thin Solid Films*. 518 (2009) 1532–1537.
- [33] L.E. Koutsokeras, G. Abadias, Intrinsic stress in ZrN thin films: Evaluation of grain boundary contribution from in situ wafer curvature and ex situ x-ray diffraction techniques, *J. Appl. Phys.* 111 (2012) 93509.
- [34] L. Chen, J. Paulitsch, Y. Du, P.H. Mayrhofer, Thermal stability and oxidation resistance of Ti--Al--N coatings, *Surf. Coatings Technol.* 206 (2012) 2954–2960.
- [35] P.H. Mayrhofer, A. Hörling, L. Karlsson, J. Sjöln, T. Larsson, C. Mitterer, L. Hultman, Self-organized nanostructures in the Ti--Al--N system, *Appl. Phys. Lett.* 83 (2003) 2049–2051.
- [36] P.H. Mayrhofer, D. Music, J.M. Schneider, Influence of the Al distribution on the structure, elastic properties, and phase stability of supersaturated Ti_{1-x}Al_xN, *J. Appl. Phys.* 100 (2006) 94906.
- [37] D. Holec, R. Rachbauer, L. Chen, L. Wang, D. Luef, P.H. Mayrhofer, Phase stability and alloy-related trends in Ti--Al--N, Zr--Al--N and Hf--Al--N systems from first principles, *Surf. Coatings Technol.* 206 (2011) 1698–1704.
- [38] A. Hörling, L. Hultman, M. Odén, J. Sjöln, L. Karlsson, Mechanical properties and machining performance of Ti_{1-x}Al_xN-coated cutting tools, *Surf. Coatings Technol.* 191 (2005) 384–392.
- [39] C. Wüstefeld, D. Rafaja, V. Klemm, C. Michotte, M. Kathrein, Effect of the aluminium content and the bias voltage on the microstructure formation in Ti_{1-x}Al_xN protective coatings grown by cathodic arc evaporation, *Surf. Coatings Technol.* 205 (2010) 1345–1349. <https://doi.org/10.1016/j.surfcoat.2010.07.057>.
- [40] S.N. Naik, S.M. Walley, The Hall--Petch and inverse Hall--Petch relations and the hardness of nanocrystalline metals, *J. Mater. Sci.* 55 (2020) 2661–2681.
- [41] N. Schalk, C. Mitterer, J. Keckes, M. Penoy, C. Michotte, Influence of residual stresses and grain size on the spinodal decomposition of metastable Ti_{1-x}Al_xN coatings, *Surf. Coatings Technol.* 209 (2012) 190–196. <https://doi.org/10.1016/j.surfcoat.2012.08.052>.
- [42] B. Syed, T.-W. Hsu, A.B.B. Chaar, P. Polcik, S. Kolozsvari, G. Håkansson, J. Rosén, L.J.S. Johnson, I. Zhirkov, J.M. Andersson, others, Effect of varying N₂ pressure on DC arc plasma properties and microstructure of TiAlN coatings, *Plasma Sources Sci. Technol.* 29 (2020) 95015.
- [43] D. Rafaja, A. Poklad, V. Klemm, G. Schreiber, D. Heger, M. Šíma, M. Dopita, Some consequences of the partial crystallographic coherence between nanocrystalline domains in Ti-Al-N and Ti-Al-Si-N coatings, *Thin Solid Films*. 514 (2006) 240–249. <https://doi.org/10.1016/j.tsf.2006.02.092>.
- [44] C. V Falub, A. Karimi, M. Ante, W. Kalss, Interdependence between stress and texture in arc evaporated Ti--Al--N thin films, *Surf. Coatings Technol.* 201 (2007) 5891–5898.
- [45] L. von Fieandt, M. Fallqvist, T. Larsson, E. Lindahl, M. Boman, Tribological properties of highly oriented Ti (C, N) deposited by chemical vapor deposition, *Tribol. Int.* 119 (2018) 593–599.
- [46] Y. Kumashiro, A. Itoh, T. Kinoshita, M. Sobajima, The micro-Vickers hardness of TiC single crystals up to 1500 C, *J. Mater. Sci.* 12 (1977) 595–601.

- [47] A.-N. Wang, G.-P. Yu, J.-H. Huang, Fracture toughness measurement on TiN hard coatings using internal energy induced cracking, *Surf. Coatings Technol.* 239 (2014) 20–27.
- [48] A. Azushima, Y. Tanno, H. Iwata, K. Aoki, Coefficients of friction of TiN coatings with preferred grain orientations under dry condition, *Wear.* 265 (2008) 1017–1022.
- [49] H. Ljungcrantz, L. Hultman, J.-E. Sundgren, L. Karlsson, Ion induced stress generation in arc-evaporated TiN films, *J. Appl. Phys.* 78 (1995) 832–837.
- [50] K. Chu, P.W. Shum, Y.G. Shen, Substrate bias effects on mechanical and tribological properties of substitutional solid solution (Ti, Al) N films prepared by reactive magnetron sputtering, *Mater. Sci. Eng. B.* 131 (2006) 62–71.
- [51] N.P.S. Chandra, Y. Otsuka, Y. Mutoh, K. Yamamoto, Fatigue strength and mechanism of Ti6242S titanium alloy with TiAlN coating deposited under various bias voltages, *Int. J. Fatigue.* 131 (2020) 105338.
- [52] J.L. Schroeder, W. Thomson, B. Howard, N. Schell, L. Näslund, L. Rogström, M.P. Johansson-Jöesaar, N. Ghafoor, M. Odén, E. Nothnagel, A. Shepard, J. Greer, J. Birch, Industry-relevant magnetron sputtering and cathodic arc ultra-high vacuum deposition system for in situ x-ray diffraction studies of thin film growth using high energy synchrotron radiation, *Rev. Sci. Instrum.* 86 (2015) 95113.
- [53] N. Shulumba, O. Hellman, L. Rogström, Z. Raza, F. Tasnádi, I.A. Abrikosov, M. Odén, Temperature-dependent elastic properties of Ti_{1-x}Al_xN alloys, *Appl. Phys. Lett.* 107 (2015) 231901.
- [54] A.L. Patterson, The Scherrer formula for X-ray particle size determination, *Phys. Rev.* 56 (1939) 978.
- [55] G. Janssen, A.J. Dammers, V.G.M. Sivel, W.R. Wang, Tensile stress in hard metal films, *Appl. Phys. Lett.* 83 (2003) 3287–3289.
- [56] E. Chason, M. Karlson, J.J. Colin, D. Magnfält, K. Sarakinos, G. Abadias, A kinetic model for stress generation in thin films grown from energetic vapor fluxes, *J. Appl. Phys.* 119 (2016). <https://doi.org/10.1063/1.4946039>.
- [57] P. Pobedinskas, J.C. Bolsée, W. Dexters, B. Ruttens, V. Mortet, J. D’Haen, J. V. Manca, K. Haenen, Thickness dependent residual stress in sputtered AlN thin films, *Thin Solid Films.* 522 (2012) 180–185. <https://doi.org/10.1016/j.tsf.2012.08.015>.
- [58] M. Beckers, N. Schell, R.M.S. Martins, A. Mücklich, W. Möller, In situ x-ray diffraction studies concerning the influence of Al concentration on the texture development during sputter deposition of Ti–Al–N thin films, *J. Vac. Sci. & Technol. A Vacuum, Surfaces, Film.* 23 (2005) 1384–1391.
- [59] G. Abadias, Y.Y. Tse, P. Guérin, V. Pelosin, Interdependence between stress, preferred orientation, and surface morphology of nanocrystalline TiN thin films deposited by dual ion beam sputtering, *J. Appl. Phys.* 99 (2006) 113519.
- [60] D. Rafaja, M. Šíma, V. Klemm, G. Schreiber, D. Heger, L. Havela, R. Kužel, X-ray diffraction on nanocrystalline Ti_{1-x}Al_xN thin films, *J. Alloys Compd.* 378 (2004) 107–111.
- [61] C. Tholander, B. Alling, F. Tasnádi, J.E. Greene, L. Hultman, Effect of Al substitution on Ti, Al, and N adatom dynamics on TiN (001), (011), and (111) surfaces, *Surf. Sci.* 630 (2014) 28–40.
- [62] D. Gall, S. Kodambaka, M.A. Wall, I. Petrov, J.E. Greene, Pathways of atomistic processes on TiN (001) and (111) surfaces during film growth: an ab initio study, *J. Appl. Phys.* 93 (2003) 9086–9094.
- [63] S. Mahieu, P. Ghekiere, D. Depla, R. De Gryse, Biaxial alignment in sputter deposited thin films, *Thin Solid Films.* 515 (2006) 1229–1249. <https://doi.org/10.1016/j.tsf.2006.06.027>.
- [64] G. Janssen, F.D. Tichelaar, C.C.G. Visser, Stress gradients in CrN coatings, *J. Appl. Phys.* 100 (2006) 93512.
- [65] N. Schell, W. Matz, J. Böttiger, J. Chevallier, P. Kringhøj, Development of texture in TiN films by use of in situ synchrotron x-ray scattering, *J. Appl. Phys.* 91 (2002) 2037–2044.
- [66] S. Spor, N. Jäger, M. Meindlhumer, H. Hruby, M. Burghammer, F. Nahif, C. Mitterer, J. Keckes, R. Daniel, Evolution of structure, residual stress, thermal stability and wear resistance of nanocrystalline multilayered Al_{0.7}Cr_{0.3}N–Al_{0.67}Ti_{0.33}N coatings, *Surf. Coatings Technol.* 425 (2021). <https://doi.org/10.1016/j.surfcoat.2021.127712>.
- [67] X.-H. Xu, H.-S. Wu, C.-J. Zhang, Z.-H. Jin, Morphological properties of AlN piezoelectric thin films deposited by DC reactive magnetron sputtering, *Thin Solid Films.* 388 (2001) 62–67.
- [68] D. Holec, P.H. Mayrhofer, Surface energies of AlN allotropes from first principles, *Scr. Mater.* 67 (2012) 760–762.
- [69] H. Cheng, Y. Sun, J.X. Zhang, Y.B. Zhang, S. Yuan, P. Hing, AlN films deposited under various nitrogen concentrations by RF reactive sputtering, *J. Cryst. Growth.* 254 (2003) 46–54.

- [70] M.G. Kendall, Rank correlation methods., (1948).
- [71] A. Dulmaa, F.G. Cougnon, R. Dedoncker, D. Depla, On the grain size-thickness correlation for thin films, *Acta Mater.* 212 (2021) 116896. <https://doi.org/10.1016/j.actamat.2021.116896>.
- [72] G. Abadias, L. Simonot, J.J. Colin, A. Michel, S. Camelio, D. Babonneau, Volmer-Weber growth stages of polycrystalline metal films probed by in situ and real-time optical diagnostics, *Appl. Phys. Lett.* 107 (2015) 183105.
- [73] D. Depla, B.R. Braeckman, Quantitative correlation between intrinsic stress and microstructure of thin films, *Thin Solid Films.* 604 (2016) 90–93. <https://doi.org/10.1016/j.tsf.2016.03.039>.
- [74] L.E. Toth, *Transition Metal Carbides and Nitrides* (Academic Press, New York, 1971)., (n.d.).
- [75] I. Petrov, P.B. Barna, L. Hultman, J.E. Greene, Microstructural evolution during film growth, *J. Vac. Sci. Technol. A Vacuum, Surfaces, Film.* 21 (2003) S117–S128. <https://doi.org/10.1116/1.1601610>.
- [76] C. V Thompson, Structure evolution during processing of polycrystalline films, *Annu. Rev. Mater. Res.* 30 (2000) 159.
- [77] G. Abadias, E. Chason, J. Keckes, M. Sebastiani, G.B. Thompson, E. Barthel, G.L. Doll, C.E. Murray, C.H. Stoessel, L. Martinu, Review Article: Stress in thin films and coatings: Current status, challenges, and prospects, *J. Vac. Sci. Technol. A Vacuum, Surfaces, Film.* 36 (2018) 020801. <https://doi.org/10.1116/1.5011790>.
- [78] T. Kaub, Z. Rao, E. Chason, G.B. Thompson, The influence of deposition parameters on the stress evolution of sputter deposited copper, *Surf. Coatings Technol.* 357 (2019) 939–946.
- [79] A.M. Engwall, Z. Rao, E. Chason, Residual Stress in Electrodeposited Cu Thin Films: Understanding the Combined Effects of Growth Rate and Grain Size, *J. Electrochem. Soc.* 164 (2017) D828–D834. <https://doi.org/10.1149/2.0921713jes>.
- [80] E. Chason, A. Engwall, F. Pei, M. Lafouresse, U. Bertocci, G. Stafford, J.A. Murphy, C. Lenihan, D.N. Buckley, Understanding residual stress in electrodeposited Cu thin films, *J. Electrochem. Soc.* 160 (2013) D3285.
- [81] A.M. Engwall, Z. Rao, E. Chason, Origins of residual stress in thin films: Interaction between microstructure and growth kinetics, *Mater. & Des.* 110 (2016) 616–623.
- [82] Z. Xu, Z. Zhang, M. Bartosik, Y. Zhang, P.H. Mayrhofer, Y. He, Insight into the structural evolution during TiN film growth via atomic resolution TEM, *J. Alloys Compd.* 754 (2018) 257–267. <https://doi.org/10.1016/j.jallcom.2018.04.268>.
- [83] B. Biswas, Y. Purandare, I. Khan, P.E. Hovsepian, Effect of substrate bias voltage on defect generation and their influence on corrosion and tribological properties of HIPIMS deposited CrN/NbN coatings, *Surf. Coatings Technol.* 344 (2018) 383–393. <https://doi.org/10.1016/j.surfcoat.2018.03.009>.
- [84] R.C. Pasianot, A.M. Monti, G. Simonelli, E.J. Savino, Computer simulation of SIA migration in bcc and hcp metals, *J. Nucl. Mater.* 276 (2000) 230–234.
- [85] S. V Starikov, Z. Insepov, J. Rest, A.Y. Kuksin, G.E. Norman, V. V Stegailov, A. V Yanilkin, Radiation-induced damage and evolution of defects in Mo, *Phys. Rev. B.* 84 (2011) 104109.
- [86] X. Zhou, X. Yu, D. Jacobson, G.B. Thompson, A molecular dynamics study on stress generation during thin film growth, *Appl. Surf. Sci.* 469 (2019) 537–552. <https://doi.org/10.1016/j.apsusc.2018.09.253>.
- [87] M. Bartosik, C. Rumeau, R. Hahn, Z.L. Zhang, P.H. Mayrhofer, Fracture toughness and structural evolution in the TiAlN system upon annealing, *Sci. Rep.* 7 (2017) 1–9.
- [88] W.M. Seidl, M. Bartosik, S. Kolozsvári, H. Bolvardi, P.H. Mayrhofer, Influence of Ta on the fracture toughness of arc evaporated Ti-Al-N, *Vacuum.* 150 (2018) 24–28.
- [89] M. Bartosik, R. Hahn, Z.L. Zhang, I. Ivanov, M. Arndt, P. Polcik, P.H. Mayrhofer, Fracture toughness of Ti-Si-N thin films, *Int. J. Refract. Met. Hard Mater.* 72 (2018) 78–82.
- [90] D.G. Sangiovanni, F. Tasnadi, L.J.S. Johnson, M. Odén, I.A. Abrikosov, Strength, transformation toughening, and fracture dynamics of rocksalt-structure $Ti_{1-x}Al_xN$ ($0 \leq x \leq 0.75$) alloys, *Phys. Rev. Mater.* 4 (2020) 33605.